Naval Research Laboratory

Washington, DC 20375-5320

NRL/MR-MM/6110--03-8663

Advanced *MTADS* Classification for Detection and Discrimination of UXO

H. H. NELSON

Chemical Dynamics and Diagnostics Branch
Chemistry Division

T. H. BELL
J. R. MCDONALD
B. BARROW

AETC, Incorporated
Arlington, VA

January 31, 2003

REPORT DOCUMENTATION PAGE

Form Approved
OMB No. 0704-0188

1. REPORT DATE *(DD-MM-YYYY)*	2. REPORT TYPE	3. DATES COVERED *(From - To)*
January 31, 2003	Final Report	

4. TITLE AND SUBTITLE

Advanced *MTADS* Classification for Detection and Discrimination of UXO

5a. CONTRACT NUMBER

5b. GRANT NUMBER

5c. PROGRAM ELEMENT NUMBER

6. AUTHOR(S)

H.H. Nelson, T.H. Bell,* J.R. McDonald,* and B. Barrow*

5d. PROJECT NUMBER

5e. TASK NUMBER

5f. WORK UNIT NUMBER
61-5802-H-1

7. PERFORMING ORGANIZATION NAME(S) AND ADDRESS(ES)

Naval Research Laboratory, Code 6110
4555 Overlook Avenue, SW
Washington, DC 20375-5320

8. PERFORMING ORGANIZATION REPORT NUMBER

NRL/MR-MM/6110--03-8663

9. SPONSORING / MONITORING AGENCY NAME(S) AND ADDRESS(ES)

Environmental Security Technology Certification Program
901 North Stuart Street
Suite 303
Arlington, VA 22203

10. SPONSOR / MONITOR'S ACRONYM(S)

ESTCP

11. SPONSOR / MONITOR'S REPORT NUMBER(S)

12. DISTRIBUTION / AVAILABILITY STATEMENT

Approved for public release; distribution is unlimited.

13. SUPPLEMENTARY NOTES

*AETC, Inc., Arlington, VA 22202
Accompanying CD (on the inside of the back cover) contains this Memoradum Report, including Appendix C; the Test Plan; and four data files.

14. ABSTRACT

The Chemistry Division of the Naval Research Laboratory has developed the Multi-sensor Towed Array Detection System (*MTADS*) for the detection and classification of buried unexploded ordnance. In order to increase the discrimination ability of the system, we have developed advanced analysis algorithms for the Electromagnetic Induction (EMI) sensor data. In order to critically test the performance of these algorithms, we performed a magnetometer and two EMI surveys of a seeded, 10-acre site on the Impact Area of the Badlands Bombing Range, SD. We quantitatively compare the predictions from a baseline *MTADS* magnetometry analysis, an advanced EMI analysis, and a probabilistic neural net approach developed in a related SERDP program against actual remediation results. In addition, we discuss the performance of the EMI system in both a low- and high-SNR environment.

15. SUBJECT TERMS

Multi-sensor Towed Array Detection System (MTADS); Electromagnetic Induction (EMI); Unexploded ordnance (UXO)

16. SECURITY CLASSIFICATION OF:			17. LIMITATION OF ABSTRACT	18. NUMBER OF PAGES	19a. NAME OF RESPONSIBLE PERSON
a. REPORT	b. ABSTRACT	c. THIS PAGE			Herbert Nelson
Unclassified	Unclassified	Unclassified	UL	64	19b. TELEPHONE NUMBER *(include area code)* (202) 767-3686

Standard Form 298 (Rev. 8-98)
Prescribed by ANSI Std. Z39.18

Contents

Figures

Tables

Advanced *MTADS* Classification for Detection and Discrimination of UXO

Naval Research Laboratory

8 October 2002

1. Introduction

1.1 Background

It is now generally recognized that unexploded ordnance (UXO) is one of the Department of Defense's most severe environmental problems. Current estimates suggest that there are nearly 6 million acres of Closed, Transferred, and Transferring Ranges contaminated with UXO. The projected cost to remediate these lands ranges from $10 to $100B. These cost estimates are based on remediation using the traditional "mag and flag" method. This technique is slow, labor intensive, and inefficient;[1] upwards of 70% of the costs of a typical "mag and flag" survey go to removal of non-UXO items and investigation of "dry holes." Even worse, because "mag and flag" is a hand method that depends on the skill and attention of individual operators, it does not result in a definable level of residual risk. Clearly, there is a role for technological developments to improve this situation.

The Environmental Security Technology Certification Program, ESTCP, supported the Naval Research Laboratory in the development of the Multi-sensor Towed Array Detection System, *MTADS,* to address these deficiencies. The *MTADS* incorporates both cesium vapor full-field magnetometers and time-domain pulsed-induction sensors in linear arrays that are towed over survey sites by an all-terrain vehicle. Sensor positioning is provided by state-of-the-art Real Time Kinematic (RTK) GPS receivers. The survey data acquired by *MTADS* are analyzed using NRL-developed Data Analysis System, DAS. The DAS was designed to locate, identify and categorize all military ordnance at its maximum self-burial depth. It is efficient and simple to operate by relatively untrained personnel.

The performance of the *MTADS* has been demonstrated at a number of prepared sites and live ranges over the past six years.[2-12] It can detect and locate ordnance with accuracies on the order of 15 cm.[5] However, even with careful mission planning and preliminary training there are still significant numbers of non-ordnance targets selected. Thus, more effective discrimination algorithms are required.

We have recently completed an ESTCP-funded program, "Electromagnetic Induction and Magnetic Sensor Fusion for Enhanced UXO Target Classification," which addressed this need.

Manuscript approved December 20, 2002

The program was based on the premise that classification based on shape is central to the problem of discriminating between unexploded ordnance (UXO) and clutter. Most UXO fit a specific profile: they are long and slender with typical length-to-diameter aspect ratios of four or five. Many clutter items, on the other hand, do not fit this profile. Using pulsed-induction sensor data, we developed a model-based estimation procedure to determine whether or not a target is likely to be a UXO item. The model relies on exploiting the dependence of the induced field on target size, shape and orientation. The results of this program were documented in a Final Technical Report[13] and a Cost and Performance Report.[14] The final demonstration of this program, while conducted on a live research range, had only a limited distribution of clutter. In order to better measure the utility of these methods on a variety of sites, we undertook this demonstration on a former gunnery range.

1.2 Official DOD Requirement Statement

The Navy Tri-Service Environmental Quality Research Development Test and Evaluation Strategic Plan specifically addresses under Thrust Requirements l.A.1 and 1.A.2, the requirements for improved detection, location and removal of UXO on land and under water. The index numbers associated with these requirements are 1.I.4.e and 1.III.2.f. The priority 1 rankings of these requirements indicate that they address existing statutory requirements, executive orders or significant health and safety issues. Specifically the requirements document states:

> *There are more than twenty million acres of bombing and target ranges under DOD control. Of particular concern for the Navy are the many underwater sites which have yet to be characterized. Each year a significant fraction (200,000-500,000 acres) of these spaces are returned to civilian (Private or Commercial) use. All these areas must be surveyed for buried ordnance and other hazardous materials, rendered certified and safe for the intended end use. This is an extremely labor intensive and expensive process, with costs often far exceeding the value of the land.... Improved technologies for locating, identifying and marking ordnance items must be developed to address all types of terrain, such as open fields, wooded areas, rugged inaccessible areas, and underwater sites*.[15]

The *MTADS* addresses all aspects of the Tri-Service Requirements for land-based buried UXO. It is designed to survey large sites rapidly and efficiently, with commensurate economic benefits. Moreover, it is capable of detecting all classes of buried UXO at their likely self-burial depths. The system will correctly locate buried targets, determine their burial depths, classify the likely ordnance size, provide for future target way pointing, as well as create GIS-compatible target output maps and sorted target tables.

1.3 Objective of the Demonstration

The objective of this Demonstration is to quantify the performance of the classification methods discussed above on a site with real-world clutter and enough targets to achieve reliable statistics. In a previous survey of the Badlands Bombing Range Impact Area,[11] a 200 x 300-m area was surveyed using the *MTADS* EM array. After completion of the survey, several of the targets

found on the site were measured in the *MTADS* test pit at Blossom Point and fit confidence statistics for the likely targets were developed. By applying these statistics to the previously obtained EM survey data, we were able to exclude most of the clutter items in the EM area from the target class. Unfortunately, there were no ordnance targets in the area chosen for the test of the EM algorithms. This, of course, limits the confidence we can place on the classification ability of the EM analysis algorithms.

In order to critically test the performance of the EM analysis algorithms, we performed a magnetometer and two EM surveys of a seeded, 10-acre site on the Impact Area. We quantitatively compare the predictions from a baseline *MTADS* magnetometry analysis, an advanced EM analysis, and a probabilistic neural net approach developed in a related SERDP program against actual remediation results. In addition, we discuss the performance of the EM system in both a low- and high-SNR environment.

2. Technology Description

2.1 Technology Development and Application

2.1.1 *MTADS* Field Hardware

The *MTADS* hardware consists of a low-magnetic-signature vehicle that is used to tow linear arrays of magnetometer and pulsed-induction sensors to conduct surveys of large areas to detect buried UXO.[16] The *MTADS* tow vehicle, manufactured by Chenowth Racing Vehicles, is a custom-built off-road vehicle, specifically modified to have an extremely low magnetic signature. Most ferrous components have been removed from the body, drive train, and engine and replaced with non-ferrous alloys.

The *MTADS* magnetometers are Cs-vapor full-field magnetometers (Geometrics Model 822ROV). Eight sensors are deployed as a magnetometer array. The time-variation of the Earth's field is measured by a ninth sensor deployed at a static site removed from the survey area. These data are used to correct the survey magnetic readings.

The pulsed-induction sensors (specially modified Geonics EM61s for the baseline system and EM61 MkIIs for this demonstration) are deployed as an overlapping array of three sensors. The sensors employed by *MTADS* have been modified to make them more compatible with vehicular speeds and to increase their sensitivity to small objects. The *MTADS* baseline EM61s have the sample gate at the earliest possible time. This enhances signal levels, and thus detection performance, but at the cost of classification ability. The EM61 MkIIs used for this Demonstration have four sample gates; two configured to match the baseline *MTADS* system (a gate sampling both the top and bottom receive coils early in the decay) and the other two sampling the bottom coil at progressively later times. This was intended to enhance our ability

to discriminate large objects from a collection of smaller fragments. The trade-offs in accomplishing this will be discussed in Section 5.

The sensor positions are measured in real-time (5 Hz) using the latest RTK GPS technology. All navigation and sensor data are time-stamped and recorded by the data acquisition computer in the tow vehicle. The Data Analysis System (DAS) employs routines to convert these sensor and position data streams into anomaly maps for analysis.

2.1.2 Data Analysis Methodology

The standard *MTADS* analysis method has been described previously.[17] The magnetometry data have been very successfully modeled using a dipole response. We routinely recover target x,y positions to within 15 cm and target depths to ± 20%.[5] Within the signal to noise ratio of the *MTADS*, we see no residual signature attributable to higher moments.[17] The pulsed-induction modeling has been less successful. The standard algorithm is based on a sphere model and does not well represent the signatures we obtain. We have discussed the deficiencies of this model and proposed an ordnance model based on a prolate spheroid.[17]

The EM61 is a time domain instrument. It operates by transmitting a magnetic pulse that induces currents in any nearby conducting objects. These currents induce secondary magnetic fields that are measured by the sensor after the transmitter pulse has ended. The sensor response is the voltage induced in the receiver coil by these secondary fields, and is proportional to the time rate of change of the magnetic flux through the coil. The sensor integrates this induced voltage over a fixed time gate and averages over a number of pulses. An illustration of the magnitude and direction of the field transmitted by the *MTADS* array is shown in Figure 1. Note that the field experienced by an object directly below the array is substantially different than an object in front of or behind the array. This allows us to get several "looks" at the target as we conduct a survey and aids greatly in our model fits.

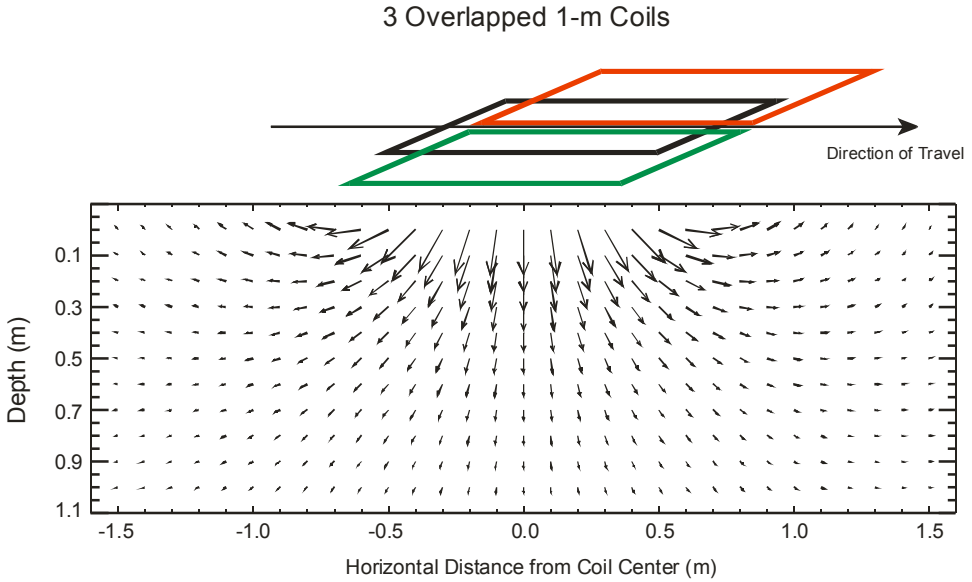

Figure 1 – Direction and magnitude of the magnetic field transmitted by the *MTADS* EM61 array

The model used in this demonstration has been jointly developed by NRL and AETC, Inc. and described at conferences and in the literature.[18,19] It relies upon the fact that the EM61 signal is a linear function of the flux through the receiving coil. The flux, assumed to originate from an induced dipole moment at the target location, is given by:

$$\mathbf{m} = \mathrm{UBU}^{\mathrm{T}} \cdot \mathbf{H}_0 \tag{1}$$

where $\mathbf{H_o}$ is the peak primary field at the target, *U* is the transformation matrix between the coordinate directions and the principal axes of the target, and *B* is an empirically-determined, effective magnetic polarizability matrix. For any arbitrary compact object, this matrix can be diagonalized about three primary body axes and written as:

$$\mathrm{B} = \begin{bmatrix} \beta_x & 0 & 0 \\ 0 & \beta_y & 0 \\ 0 & 0 & \beta_z \end{bmatrix}. \tag{2}$$

For an axisymmetric object, *B* has only two unique coefficients, corresponding to the longitudinal (β_l) and transverse (β_t) directions:

$$\mathrm{B} = \begin{bmatrix} \beta_l & 0 & 0 \\ 0 & \beta_t & 0 \\ 0 & 0 & \beta_t \end{bmatrix} \tag{3}$$

Empirically, we observe that for elongated ferrous objects such as cylinders and most UXO, the longitudinal coefficient is greater than the transverse coefficient. For flat ferrous objects such as disks and plates, the opposite is true. This matches the behavior of these objects in the magnetostatic limit. For non-ferrous objects such as aluminum cylinders and plates, these relationships are reversed.

In earlier demonstrations of this method, we have determined that conducting two orthogonal EM surveys and fitting the data using a full three-β, three-angle model yields the optimum results.[13] This survey methodology was also used in this Demonstration.

2.2 Previous Testing of the Technology

The analysis methodology described above has been demonstrated on two live-fire ranges. The Final Demonstration of ESTCP Project 199812 was conducted on 'L' Range, a mortar test range, at the Army Research Laboratory's Blossom Point Facility.[13] In this test, we were able to eliminate greater than 50% of the false alarms without impacting detection performance when we focused on a single ordnance item, 81-mm mortars. This classification performance was

degraded when attempting to detect ordnance ranging in size from fuzes to 5-in rockets but we were still able to eliminate ~20% of the false alarms.

The second demonstration of these EMI analysis methods was in conjunction with an *MTADS* survey of the Impact Area of the Badlands Bombing Range.[11] In this demonstration, which was primarily a magnetometer survey, a 200 x 300-m area was surveyed using the *MTADS* EM array. Based on the EM survey, 109 targets were fit and marked for remediation. The results of the fits are illustrated graphically in Figure 2. In this 2-D representation of the 3-D fit results, the largest, or primary, β is plotted on the x-axis and the average of the other two, or secondary, β's is plotted on the y-axis. This allows a convenient visualization of the data although all classification calculations are carried out in full 3-D.

Also plotted in Figure 2 are statistical predictions for the locations in 3-β space of the ordnance items expected to be present on the Retained Area, 105-mm, 155-mm, and 8-in projectiles. These predictions were developed after the fact from multiple measurements over each of the items in the *MTADS* test pit at Blossom Point. The ellipses correspond to 1-σ, 2-σ, and 95% fit probabilities for each item. From the 2-D representation in the figure one can immediately exclude many of the targets from the anomaly class, even a number of those with characteristic dimension similar to the ordnance items. In the 3-D view, things are even better. Many of the clutter items that appear to overlap in the 2-D representation have very different secondary β's while the ordnance items, being axisymmetric, have nearly identical responses. In the 3-D view there are only 9 (of the 109) targets within the 95% confidence ellipses for the three ordnance items.

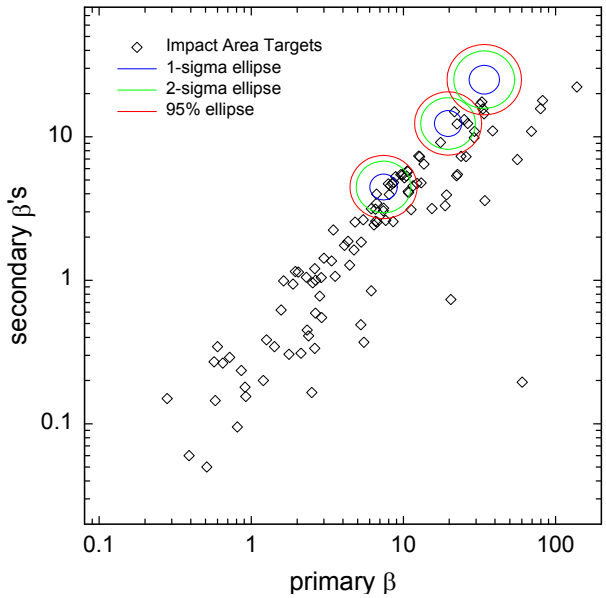

Figure 2 – Results of a 3-β analysis of the 109 targets selected from the EM area of the BBR Air Force Retained Area. For a description of the plot, see the text. The diamonds represent the targets and the ellipses are statistical predictions based on test-pit measurements

This clutter rejection, while suggestive of improved classification performance, is rendered suspect by the realization that there were no intact ordnance items in the EM survey area. That is the rationale for this second Demonstration on an area with 25 seeded targets.

2.3 Factors Influencing Cost and Performance

Implementation of the methods used in this Demonstration requires additional survey time compared to a minimum detection survey. We have shown that, in many cases, the *MTADS* can detect essentially all UXO with a total-field magnetometry survey. For ordnance target sets that include 60- and 81-mm mortars at depths of 0.75 to 1 m and/or 20- and 30-mm submunitions an overlapping EM induction survey is required to get a high detection probability. With the current *MTADS* EM array configuration, we require two orthogonal EM surveys to ensure sufficient "illumination" of each target to get a reliable fit to the model used in this Demonstration. This increases the survey hours on-site although it does not impact the mobilization and data analysis costs. In many cases, the extra survey costs are only equivalent to the cost of digging one or two additional targets per acre.

2.4 Advantages and Limitations of the Technology

No single method currently available provides the "magic bullet" of classification. We have already demonstrated[5,7] that an impressive level of discrimination is possible using the standard *MTADS* if a small training area is investigated prior to data analysis on the entire site and the distribution of ordnance is limited. This discrimination is based primarily on fitted dipole "size" and analyst impressions. The methods to be demonstrated here are designed to add an extra "dimension" to the discrimination, that of "shape." For items with the same induced magnetic dipole we can discriminate based on the ratio of responses of the items three axes to the EM induction sensors in the *MTADS* suite. As we have shown,[13] this adds some discrimination capability to the system.

Even with the most optimistic result however, these methods will not result in a perfect system. As we have stated above, this program is based on the concept of classification by shape. By definition, this implies that clutter items that have similar shapes to ordnance will be classified as ordnance. Items such as pipes and post sections are representative of this problem. If it is important to reduce remediation costs to the extent that these items are not dug, other methods, possibly sensitive to composition or the presence of explosive compounds, will have to be employed in conjunction with those being demonstrated in this program.

3. Site Description

3.1 Background

In 1999 we conducted a demonstration survey on the Impact Area (previously refered to as the Air Force Retained Area) on the Badlands Bombing Range, BBR.[11] In preparation for this work, NRL conducted site visits, records searches, Tribal coordination activities, acquisition of aerial photography and pre-surveying of first-order control points to support the activity.

This site is ideal for the purposes of this demonstration. It has been used for years for gunnery practice and is thus covered with fragments ranging from small to large. It has a number of fragment clusters that apparently result from underground explosion of practice projectiles. These fragment clusters have magnetic signatures virtually indistinguishable from that of an intact 105mm projectile. Thus, if there is value in these analysis methods, it can be demonstrated at this site.

3.2 Test Site History/Characteristics

In 1942 the Department of War annexed 341,725 acres of the Pine Ridge Reservation for use as an aerial gunnery and bombing range. This site is located in the Southwest corner of South Dakota, with the largest part of the Bombing Range located in Shannon County. From 1942 until 1948 various sections of this range were used for bombing exercises and various air to ground operations. Since 1960, portions of the land have been returned to the Oglala Sioux Tribe, OST in a step-wise fashion. In 1968, Congress enacted Public Law 90-468 returning 202,357 acres to the OST, and setting aside 136,882 acres of formerly held Tribal lands to form the Badlands National Monument, to be managed by the National Park Service. In 1978, all remaining BBR lands were declared excess with the exception of 2,486 acres, referred to as the Impact Area. In about 1965 the South Dakota National Guard placed up to 100 car bodies on the 2,486-acre area and began using them as artillery targets during training exercises. The National Guard training exercises took place on the IA between 1966 and 1973.

3.2.1 Previous UXO Clearances

There have been 6 documented UXO clearance operations on the BBR taking place between 1948 and 1997. These are discussed in more detail in Ref. 20. Only two have significant relevance to the present demonstration on the IA.

3.2.1.1 The 1975 Clearance During the summer and fall of 1975 ten EOD personnel participated in a searchline walking clearance of 22,403 acres and a vehicular search of 19,222 acres. This included a walking searchline survey of the entire IA and the buffer zone. With the exception of the IA, all lands were declared as cleared and certified for return to the Tribe. The IA apparently contained too much OE material to declare the area “cleared.” The 1975 Certificate of Clearance describes the plowing of 1,088 acres of the IA using ripper plows to clear buried ordnance. Aerial photographs clearly show that the plowing took place after 24 July

1976.[20] The Clearance Report documents recovery of the items listed below without specifying which of these items were associated with the IA.

- 5 - 155-mm Howitzer projectiles
- 3 - 155-mm illumination projectiles
- 1 - 8-in Howitzer projectile
- 1 - 10-lb Spotting Charge
- 2 - 155-mm Illumination Candles
- 4 - Smoke Grenades
- 15 - 50 Cal Cartridges
- 46 - 100-lb Practice Bombs

3.3.1.2 The 1997 Clearance During the 4-month summer period, a walking and driving searchline ordnance clearance was conducted by 20 EOD personnel operating from Ellsworth AFB.[20] With the exception of 56 acres of rugged terrain along the White River, the entire IA was covered. EOD teams used metal detectors (mine detectors) to search for buried metal. The objective was to clear the area to a depth of 1.5 feet. The OE scrap recovered included 4,000 lbs of shrapnel (pieces larger than 3 inches). An additional 8,000 lbs of non-ordnance related metal scrap was recovered, including 6 car bodies, a washing machine, barbed wire and fencing material. Live ordnance items that were blown in place are enumerated below.

- 3 - 20-mm aircraft gun ammunition
- 1 - 50 Caliber Projectile
- 1 - 105-mm High Explosive Howitzer Round
- 3 - 155-mm High Explosive Projectiles
- Inert Components of a 155-mm Illumination Projectile

3.3.1.3 The 1999 *MTADS* Clearance During the NRL Demonstration in 1999, only 155-mm and 8-in projectiles were recovered. A substantial amount of OE scrap associated with 105-mm detonations was also recovered. No evidence of other ordnance use on the site was seen.

3.2.2 Site Maps and Photographs

Figure 3 is a portion of a USGS 7.5-minute topo map showing the location of the Retained Area outlined in red. The Retained Area Range is surrounded by a buffer zone generally of about 1000 meters. The Retained Area perimeter fence is shown in red, portions of the buffer boundary are in green. A second perimeter fence is located at the outer border of the buffer zone. The most direct access to the Retained Area is by a dirt road that exits to the south from Highway 40. The dirt road was graded, including installation of some culverts, to support the 1997 EOD clearance activities. There is only one fence internal to the Retained Area. This east-west fence bisects sections 29 and 30 and is labeled “cross fence” in Figure 3. Three geodetic survey points are located on the Retained Area. These sites, labeled North BM, East BM, and

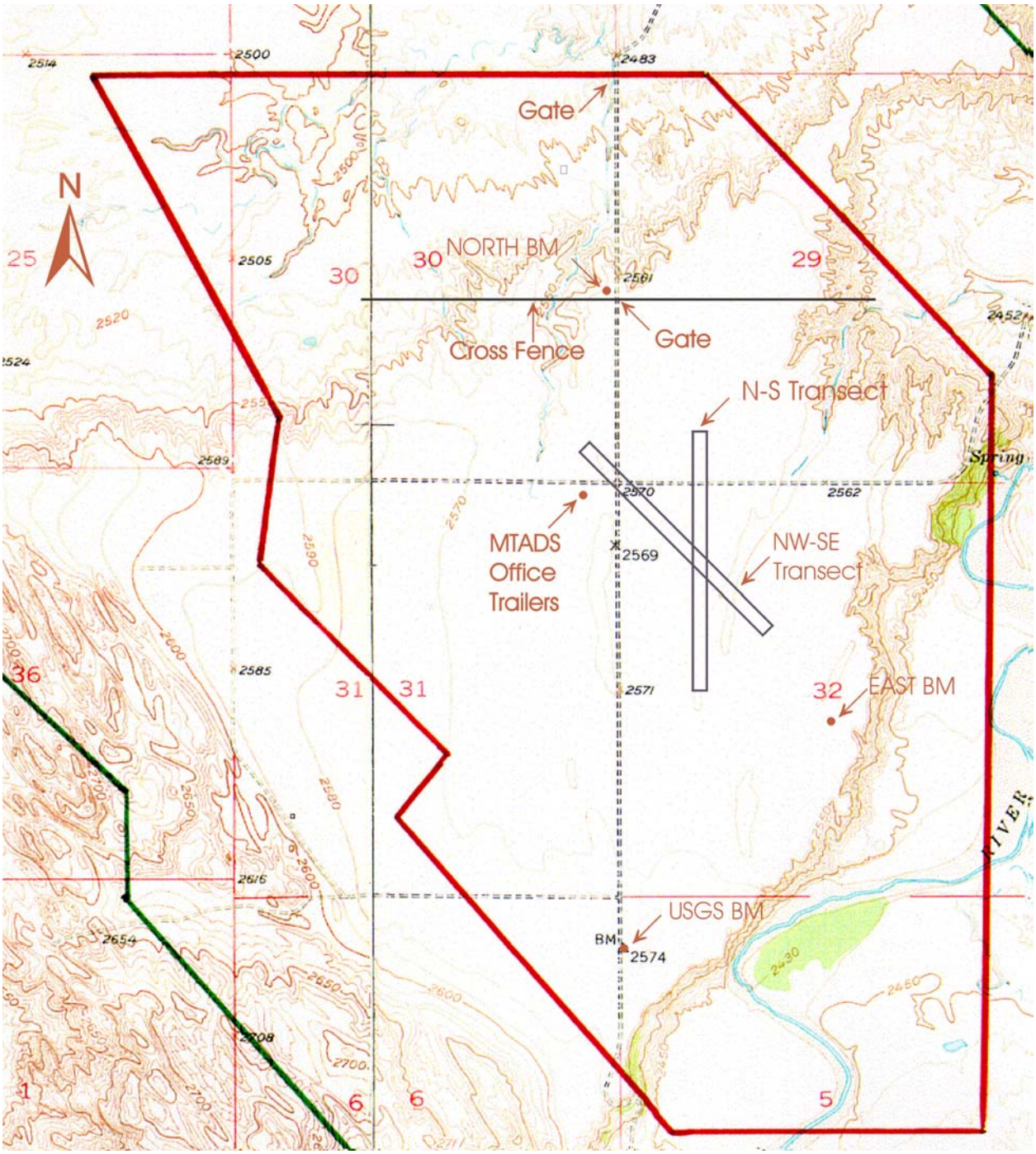

Figure 3 – A portion of a USGS 7.5-minute map with the perimeter of the Air Force Retained Area shown in red. Survey control points, transect surveys, and logistics support trailers as deployed for the 1999 MTADS survey are indicated.

USGS BM were upgraded to "near first-order" by Ellsworth AFB CES personnel using the OST 5 benchmark. The latter point was established by NRL contractors in 1997 and is legitimately first order. All 1999 NRL surveys were done using the North BM coordinates provided by Ellsworth AFB. The coordinates of each of these points are given in Table 1.

Table 1. Impact Area Survey Coordinates Provided by Ellsworth AFB.

Point	Latitude	Longitude	Northing (m)	Easting (m)	Height (m)
			NAD 83		
OST 5	43° 42' 05.2702"	-102° 18' 35.5186"	4842233.05	716761.31	804.460
North BM	43° 40' 19.1197"	-102° 14' 20.5113"	4839145.82	722578.26	762.530
East BM	43° 39' 21.2053"	-102° 13' 42.8268"	4837387.2	723481.89	764.260
USGS BM	43° 38' 53.7820"	-102° 14' 18.7564"	4836514.29	722705.23	765.940

A magnetic anomaly image map of the area surveyed by the *MTADS* vehicular system in 1999 is shown in Figure 4. The location of the survey benchmarks, the section roads and the area seeded with inert ordnance are shown.

4. Demonstration Approach

4.1 Performance Objectives

This Demonstration involved three *MTADS* vehicular surveys. First, a magnetometer survey of ten seeded acres east of the previously-identified bull's eye on the Impact Area, second, an EM61 MkII survey of the same area and, finally, an EM61 MkI survey of the area. Coincident with this Demonstration, we performed a magnetometer survey of an additional 100 acres to serve as a ground truth area for the *MTADS* Airborne Demonstration.

The survey data from the first three surveys were analyzed in the following ways:

- *MTADS* baseline analysis (only magnetometer data),
- 3-β analysis using each of the EM data sets,
- Airborne *MTADS* magnetometer analysis, and
- Probabilistic Neural Net (PNN) analysis (from the NRL SERDP Program) using baseline *MTADS* magnetometer predictions.

The Airborne analysis has already been presented[21] and will not be discussed further here.

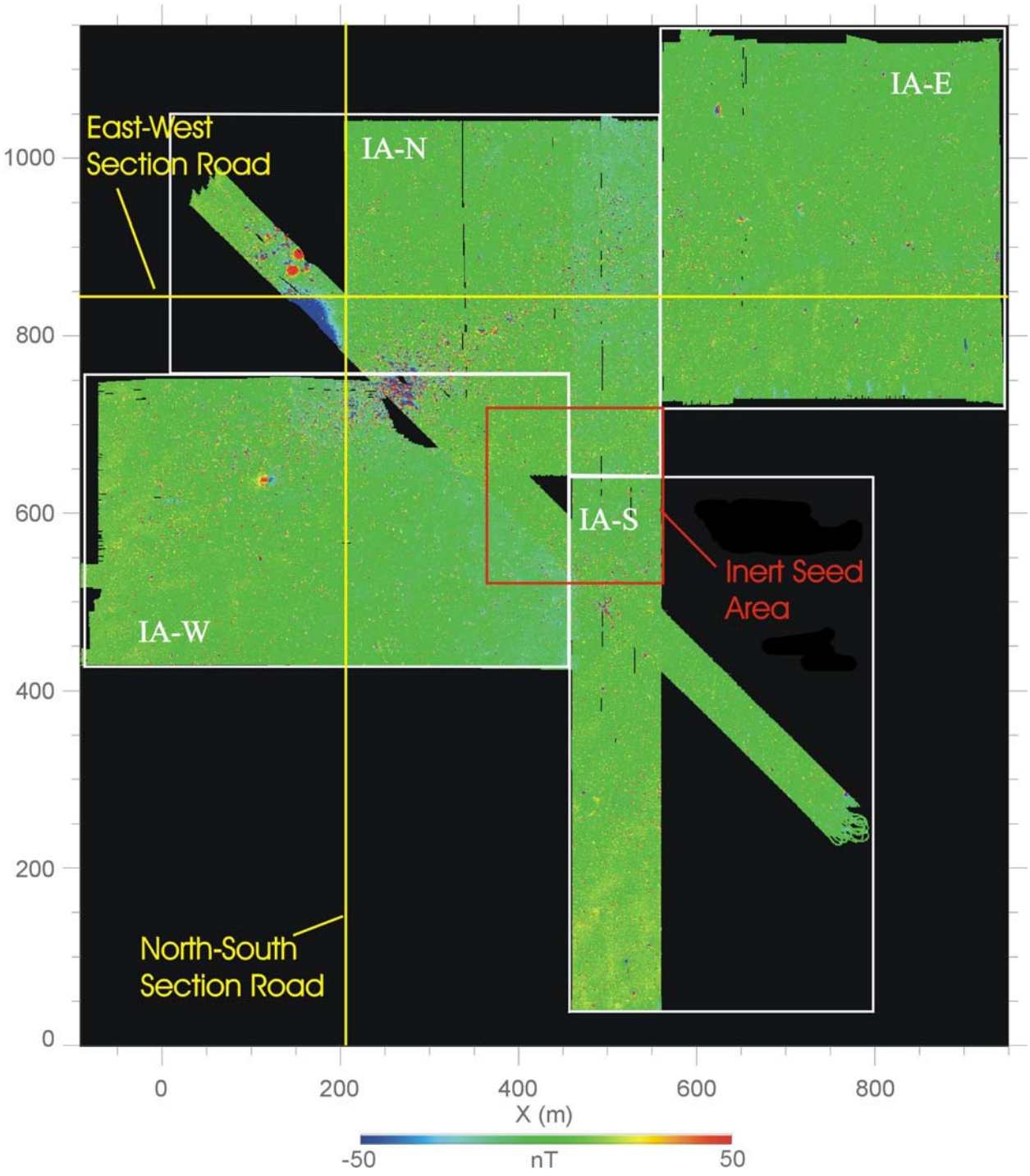

Figure 4 – Map of areas surveyed by the *MTADS* vehicular magnetometer system in 1999 showing the location of the seed area for this Demonstration

The specific objective of this Demonstration was to produce a quantitative comparison among the data analysis methodologies listed above including probability of detection and false alarm rate. After initial analysis of the data, we were able to add a comparison of the performance of the EM61 sensor array in low- and high-SNR environments to this list. We also developed alternative discrimination methods that show more promise under these conditions. All of these topics are addressed in the following section.

4.2 Physical Setup and Operation

4.2.1 Seed Targets

Inert ordnance from the Aberdeen Test Center (ATC) APG, MD was used to establish the seed area. ATC degaussed the ordnance and transferred it to ERDC in Vicksburg, MS for emplacement on the site. Mr. Tommy Berry of ERDC emplaced the inert targets on the site in August 2001. The seed area corners were provided to ERDC by NRL. The targets were emplaced using a slanted auger so there would be no visible surface scars above the ordnance. The ground truth for the seeded targets was held by ERDC until after the completion of the survey. It was not available to any individual data analyst until the completion of their assigned analyses. Table 2 contains a list of the seed target locations and orientations.

The seed target area is within a few hundred meters of the bull's eye identified in the 1999 survey and, therefore, has a high concentration of fragments and scrap (primarily pieces of auto parts from the target) on and near the surface. This provides a stringent test for the methods being demonstrated. We will discuss in Section 5 the influence on classification of this high noise field.

Table 2 – Location of the Emplaced Seed Targets at the Impact Area

Item #	Northing (m)	Easting (m)	Depth (m)	UXO Type	Azi. (°)	Incl. (°)	Nose U/D	Serial No.
1-2	4,838,171.34	722,824.74	0.75	8-inch	350	75	D	4
1-4	4,838,142.67	722,957.56	0.50	8-inch	270	45	D	5
1-6	4,838,117.82	722,874.46	0.75	8-inch	40	80	D	3
1-8	4,838,082.55	722,834.30	0.30	8-inch	10	0	H	6
1-10	4,838,019.39	722,889.76	0.50	8-inch	340	40	D	2
1-12	4,838,120.88	722,786.50	0.85	155-mm	0	45	D	10
1-14	4,838,086.48	722,802.76	0.25	155-mm	250	65	D	8
1-16	4,838,176.31	722,813.27	0.60	155-mm	15	80	D	12
1-18	4,838,143.69	722,819.03	0.85	155-mm	115	45	D	11
1-20	4,838,066.32	722,848.56	0.25	155-mm	165	70	D	13

Item #	Northing (m)	Easting (m)	Depth (m)	UXO Type	Azi. (°)	Incl. (°)	Nose U/D	Serial No.
1-22	4,838,142.69	722,860.13	0.25	155-mm	110	0	H	15
1-24	4,838,168.67	722,886.90	0.30	155-mm	360	35	D	9
1-26	4,838,106.46	722,901.24	0.55	155-mm	75	45	U	14
1-28	4,838,202.03	722,921.32	0.60	155-mm	30	40	D	6
1-30	4,838,137.07	722,919.42	0.40	155-mm	310	55	D	7
1-32	4,838,196.19	722,853.42	0.25	105-mm	110	35	D	16
1-34	4,838,176.23	722,831.42	0.92	105-mm	5	75	D	9
1-36	4,838,174.21	722,879.23	0.40	105-mm	115	45	D	10
1-38	4,838,164.65	722,931.82	0.25	105-mm	30	0	H	7
1-40	4,838,141.72	722,893.58	0.50	105-mm	50	55	D	13
1-42	4,838,118.78	722,830.47	0.60	105-mm	245	75	U	15
1-44	4,838,070.04	722,926.09	0.50	105-mm	65	60	D	12
1-46	4,838,064.41	722,957.64	0.25	105-mm	315	80	D	11
1-48	4,838,050.93	722,914.61	0.30	105-mm	25	35	D	8
1-50	4,838,032.77	722,808.48	0.30	105-mm	360	45	D	14
Corners								
NW	4,838,214.74	722,778.78						
NE	4,838,214.73	722,978.77						
SE	4,838,014.77	722,978.76						
SW	4,838,014.73	722,778.79						

4.2.2 Logistics

No logistics support was available on site. Thus, all support equipment had to be rented in Rapid City, SD and trucked 75 miles to the Impact Area site. Figure 6 is an aerial photo of the *MTADS* base camp set up just south of the cross fence shown in Figure 5 and east of the Section Road. One of the office trailers served as a data analysis and electronics repair office, the next was used for equipment storage and battery charging, the next supported the tribal workers and remediation contractors and the final, drive-through, trailer housed the vehicular *MTADS* tow vehicle and trailers. Also shown in the photo is a tent set up to provide cover from the elements during work breaks and repair and maintenance of the vehicle and sensor trailers and the tractor-trailer that is used to transport the equipment to the site from our base in Blossom Point, MD. The tank truck at the southern end of the camp was used to support the concurrent airborne

MTADS survey of the site. Finally, the diesel generator and portable toilets are shown to the east of the office trailers.

Figure 5 – Aerial photograph of the logistics support for this Demonstration

4.2.3 On-Site Labor

Because there were two nearly-concurrent Demonstrations taking place at the Impact Area, there were more personnel on site than the minimum required to accomplish the surveys described here. During the first two weeks on site, when only this Demonstration was underway, there were five *MTADS* personnel from NRL, AETC, Inc, and Nova, Inc. on-site. This is one more than the number required to comfortably carry out the survey. These personnel were broken down as two data analysts, the primary vehicle operator (who is EOD certified and served as the primary site safety officer), a field supervisor/backup operator, and an extra person who split his time between the field and data analysis. In practice, the extra person allowed us to complete many of the pre-survey tasks (marking survey blocks, mapping the perimeter of the field, etc.) for the airborne survey.

In addition to the personnel mentioned above, three to five Tribal members from the Badlands Bombing Range Project Office supported the vehicular surveys. Two of these Tribal members who are EOD certified remained on site during the remediation portion of the work to support the dig teams. The target way pointing and remediation were carried out by Explosives Ordnance Technology, Inc. (EOTI) staff. The four employees of EOTI, along with the two members of the Tribe, assembled themselves into two dig teams for the remediation.

4.2.4 Demonstration Activity Log

An activity log for this Demonstration is contained in Table 3. There were several delays associated with equipment breakdowns that were exacerbated by the airline and shipping delays associated with the events of Sept 11th. Ultimately, these delays had no significant impact on the

Demonstration, as we were required to wait for the airborne system's arrival that suffered the same delays.

Table 3 – Activity Log for the Demonstration

Date	Activity	Comment
Thu, Sept 6th	*MTADS* equipment arrives on aite	
Fri, Sept 7th	Equipment unpacked and assembled	
Sun, Sept 9th	Survey personnel arrive on site	
Mon, Sept 10th	Begin EM61 MkII calibration	Hardware failure; electronics shipped to Canada for repair
Tues, Sept 11th	Begin magnetometer survey of Seed Area	
Wed, Sept 12th	Complete Seed Area survey, begin airborne support areas	
Sat, Sept 15th	Complete vehicular magnetometer surveys	
Mon, Sept 17th	Begin EM61 MkI calibration	Center sensor fails, return to Canada for repairs
Tues, Sept 18th	EM61 MkI survey of Seed Area without center sensor	EM61 MkII returns
Wed, Sept 19th	Re-install EM61 MkII following repairs	
Thu, Sept 20th	EM61 MkII N/S survey of Seed Area	
Fri, Sept 21st	EM61 MkII E/W survey of Seed Area	EM61 MkI returns
Sat, Sept 22nd	EM61 MkI E/W survey of Seed Area	
Sun, Sept 23rd	EM61 MkI N/S survey of Seed Area	
Mon, Oct 1st	Dig teams waypoint Seed Area	
Fri, Nov 23rd	Remediation complete	

5. Performance Assessment

5.1 Performance Data

5.1.1 Pre-Demonstration Measurements

As this Demonstration was being planned, the manufacturer of the EM61, Geonics Ltd., announced a new version of the sensor, designated the EM61 MkII. This new sensor has the ability to sample the decay of the induced magnetic fields with four independent gates compared to the two gates (one each on the upper and lower receive coils) in the EM61 MkI. This new product opens the possibility of gaining extra discrimination information by sampling a portion of the time-history of the object response coefficients, β. We decided to incorporate this new instrument into the Demonstration to test the utility of these new sampling gates.

The first step in incorporating the instrument into the *MTADS* suite of sensors was to specify the temporal positions of the gates. The instrument can be configured in one of two modes; all four gates on the lower receive coil or one on the upper coil and three on the lower. In order to maintain backward compatibility of the data with the EM61 MkI data, we elected to use the second mode with the sampling gate on the upper coil and the first sampling gate on the lower coil at the same time as the *MTADS* EM61 MkI gates.

In order to gather the information required to make an intelligent choice for the later two gates in the MkII array, we leased an EM63 from Geonics for use at our Blossom Point Test Site. The EM63 can record the induced field decay in 26 time gates ranging out to beyond 20 ms. This instrument is not very amenable to vehicular use due to its low measurement rate but it ideal for accurately determining the complete decay response of test targets. We made measurements on the three projectiles expected to be encountered at the Badlands Bombing Range Impact Area, 8-in, 155-mm, and 105-mm, as well as two frag "clusters" constructed by attaching pieces of frag recovered from the Impact Area in 1999 to Styrofoam blocks to approximate the volume of the clusters encountered at the Impact Area.

An example of the data collected on a 105-mm projectile is shown in Figure 6. These data are eight of the time gates collected during a traverse over a horizontal 105-mm projectile 66 cm below the sensor. The results are color coded into two classes, red for data from the four decay times that correspond to the sampling gates used in the standard MkII with four gates on the lower coil and blue for later gates. As can be seen from the figure, the shape of the response only begins to change clearly for decay times greater than 2 ms. This change in shape is the result of longer-lived modes beginning to predominate as the short-lived modes decay. This is shown more clearly in Figure 7, which is the time-dependence of the calculated βs and their ratio obtained from a decay curve collected directly above the same object. The transition from power-law to exponential decay does not occur until decay times near 10 ms; earlier for the transverse response than the longitudinal which is evidenced by the inflection in the plot of β_L/β_T.

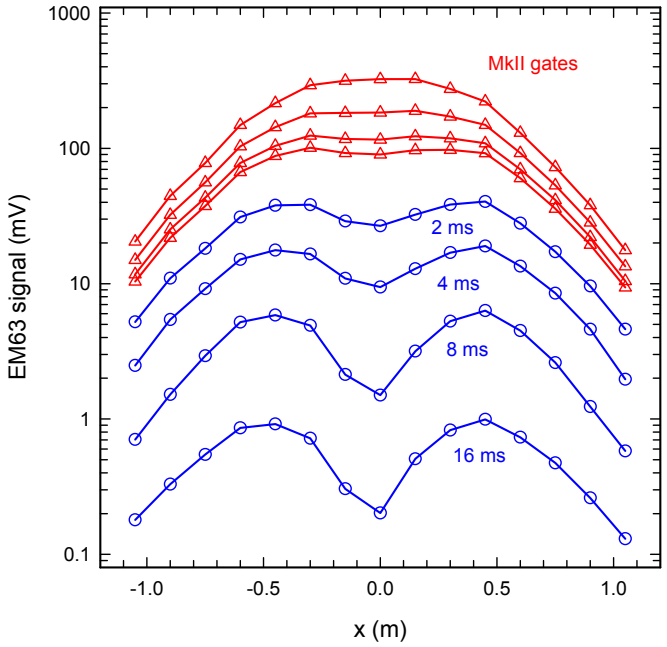

Figure 6 – Measured EM63 response profiles at eight time gates from a traverse over a horizontal 105-mm projectile 66 cm below the sensor

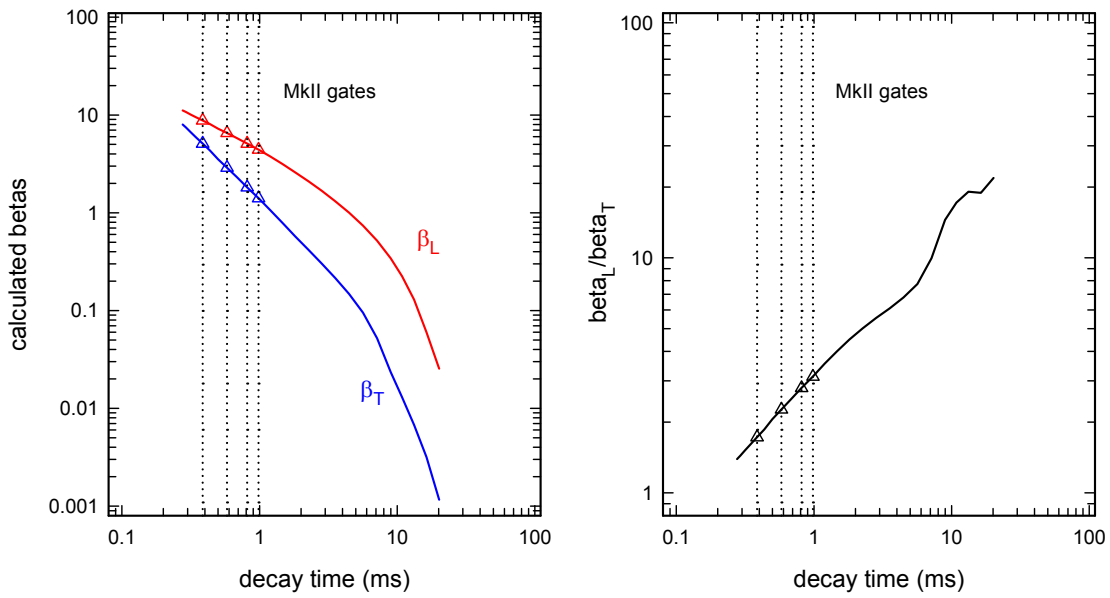

Figure 7 – Time dependence of the calculated βs (left panel) and their ratio (right panel) obtained from a decay curve collected directly above the 105-mm projectile from Figure 6

Corresponding results for a frag "cluster" are shown in Figures 8 and 9. Notice that in this case there is less variation of beta ratio with time. This is presumably because the measured response arises from the sum of many modes that decay with a range of decay times.

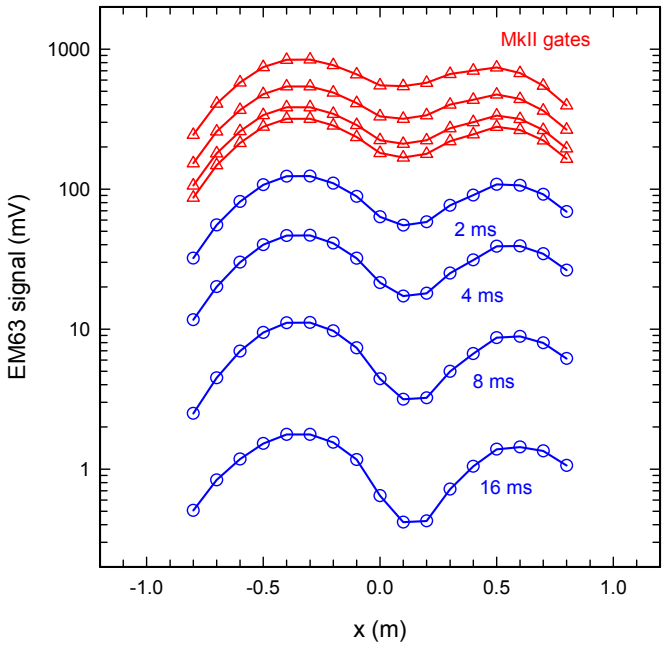

Figure 8 – Measured EM63 response profiles at eight time gates from a traverse over a frag "cluster

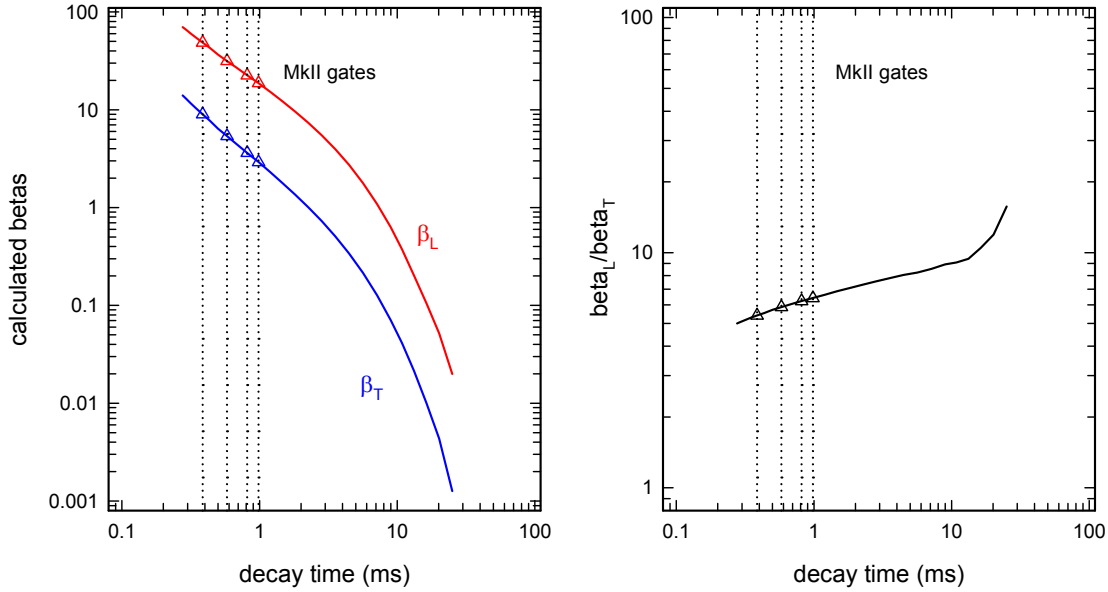

Figure 9 – Time dependence of the calculated βs (left panel) and their ratio (right panel) obtained from a decay curve collected directly above the frag "cluster" from Figure 8

Based on our measurements with the EM63, we initially specified a time for the latest gate in the *MTADS* EM61 MkII array of 2-5 ms. This number was a compromise between classification value which increases with increasing delay and S/N which decreases as the antenna repetition rate is lowered to allow for later decay measurements. Unfortunately, due to some limitations of the design of their drive electronics, the latest gate Geonics could offer with an antenna repetition rate of 150 Hz was 1.2 ms. Rather than suffer the S/N consequences of lowering the repetition rate by a factor of 2, we settled for this relatively short gate for this Demonstration. The actual gates available in the *MTADS* array for the two operating modes are listed in Table 4.

Table 4 – Gate Times for the Two Modes of the *MTADS* EM61 MkIIs

Operating Mode	"4 on lower"	"1 + 3"
Upper Coil – Gate 1		280-465 μs
Lower Coil – Gate 1	280-465 μs	280-465 μs
Lower Coil – Gate 2	465-680 μs	
Lower Coil – Gate 3	680-925 μs	680-925 μs
Lower Coil – Gate 4	925-1205 μs	925-1205 μs

5.1.2 Demonstration at the Badlands Bombing Range Impact Area

5.1.2.1 Magnetometer Measurements A conventional *MTADS* magnetometer survey of the Seed Area was conducted as the first survey at the Demonstration site. An anomaly image from this survey is shown in Figure 10 with the seeded and one live target marked. Following analysis using the *MTADS* Data Analysis System, 170 targets were marked for remediation. Following the practice of the JPG V Demonstration, the targets were classified using a six-bin scheme where category one corresponds to high confidence ordnance, category two is medium confidence ordnance, category three is low confidence ordnance, category four is low confidence clutter, category five is medium confidence clutter, and category six is high confidence clutter. The analysts attempted to scale their rankings such that digging all category 1–5 targets would completely clear UXO from the site. A summary of the analysis results is shown in Table 5. These results serve as a baseline against which to compare the performance of the EM61 systems as well as the *MTADS* airborne system.

Table 5 – Summary of the Magnetometer Analysis Results

Category	1	2	3	4	5	6	Total
Number of Targets	24	15	36	3	37	55	170

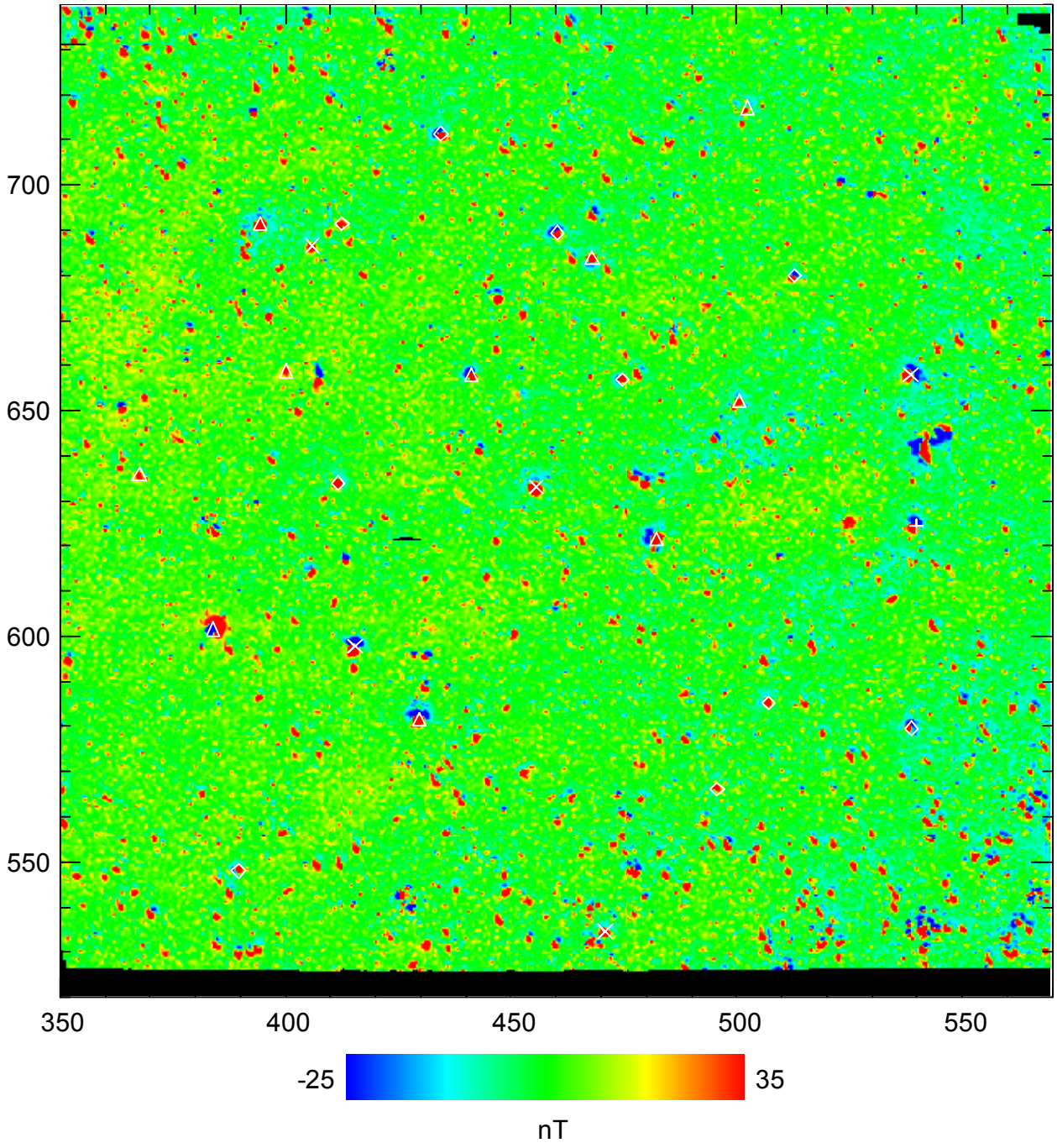

Figure 10 – Magnetic anomaly image map of the Seeded Area at the BBR Impact Area. The projectile targets are marked, diamonds for 105-mm, triangles for 155-mm, X for 8-in, and + for the live 155-mm.

5.1.2.2 EM61 MkII Measurements Both a North-South and an East-West EM61 MkII survey of the Seed Area were conducted as part of this Demonstration. A series of anomaly image maps corresponding to the four gates from the N/S survey are shown in Figures 11 - 14. As can be seen, the images look very similar. This is discussed in the next section.

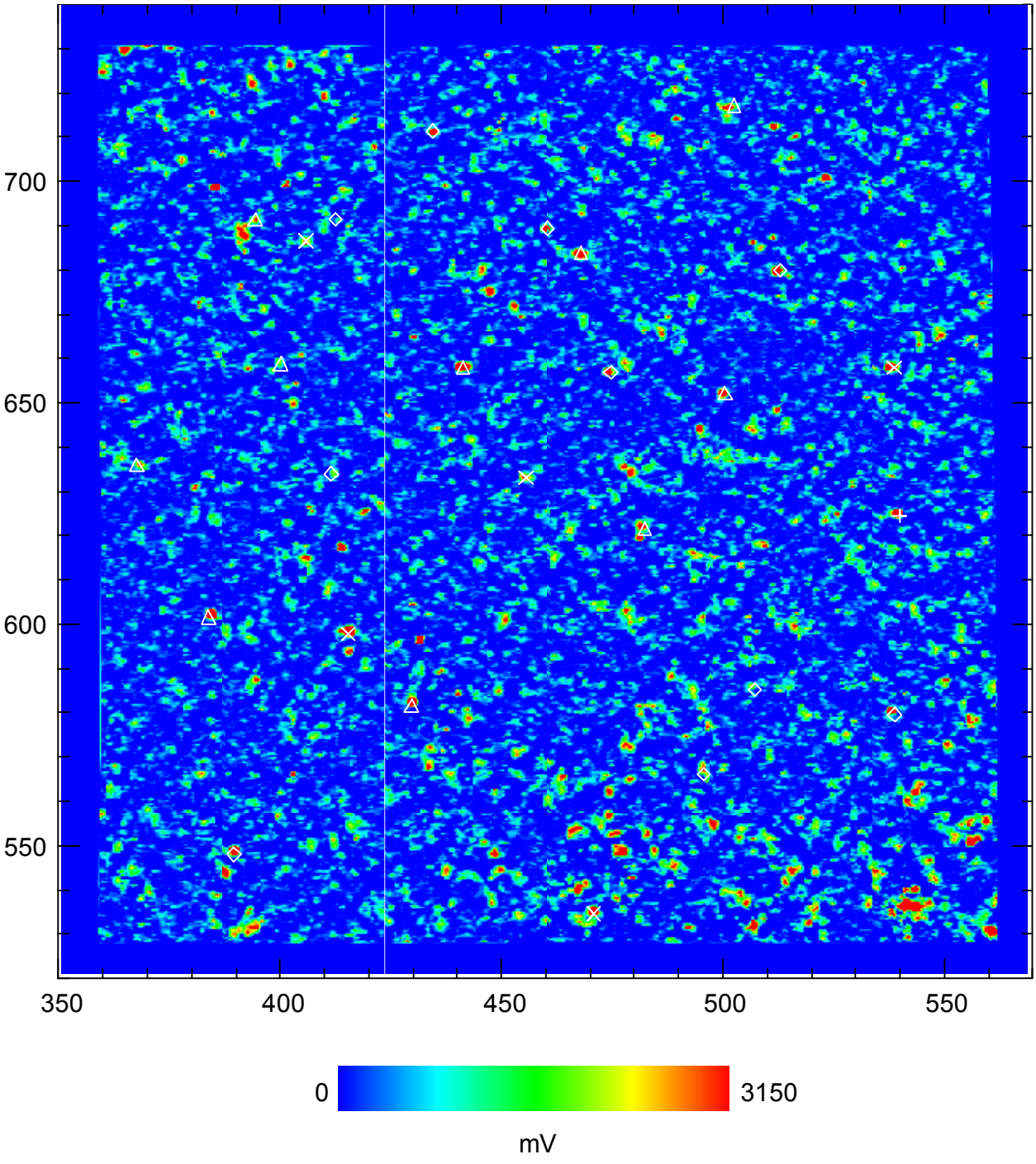

Figure 11 – EM61 MkII upper coil anomaly image map of the Seeded Area at the BBR Impact Area. The projectile targets are marked, diamonds for 105-mm, triangles for 155-mm, X for 8-in, and + for the live 155-mm.

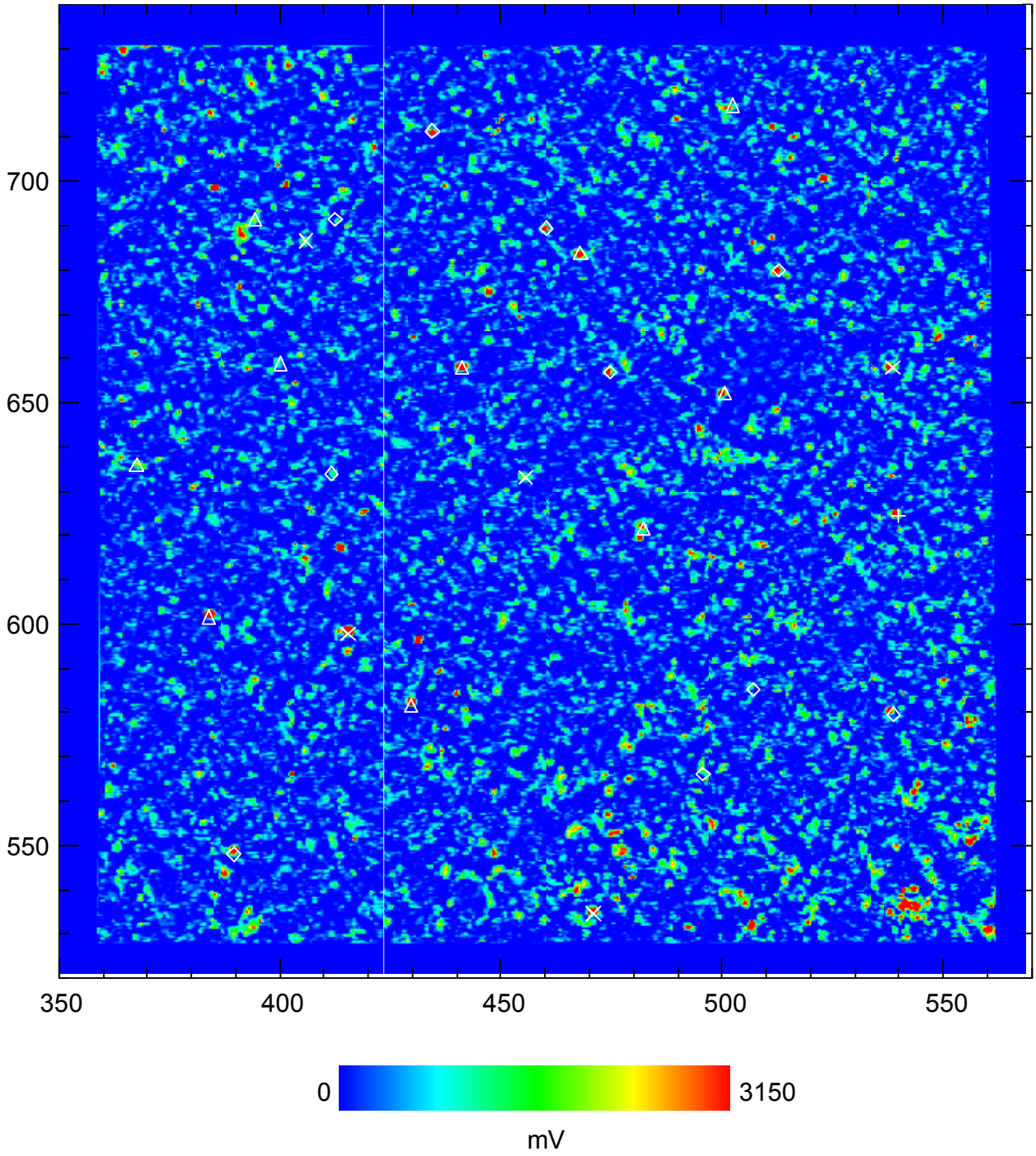

Figure 12 – EM61 MkII lower coil gate 1 anomaly image map of the Seeded Area at the BBR Impact Area. The projectile targets are marked, diamonds for 105-mm, triangles for 155-mm, X for 8-in, and + for the live 155-mm.

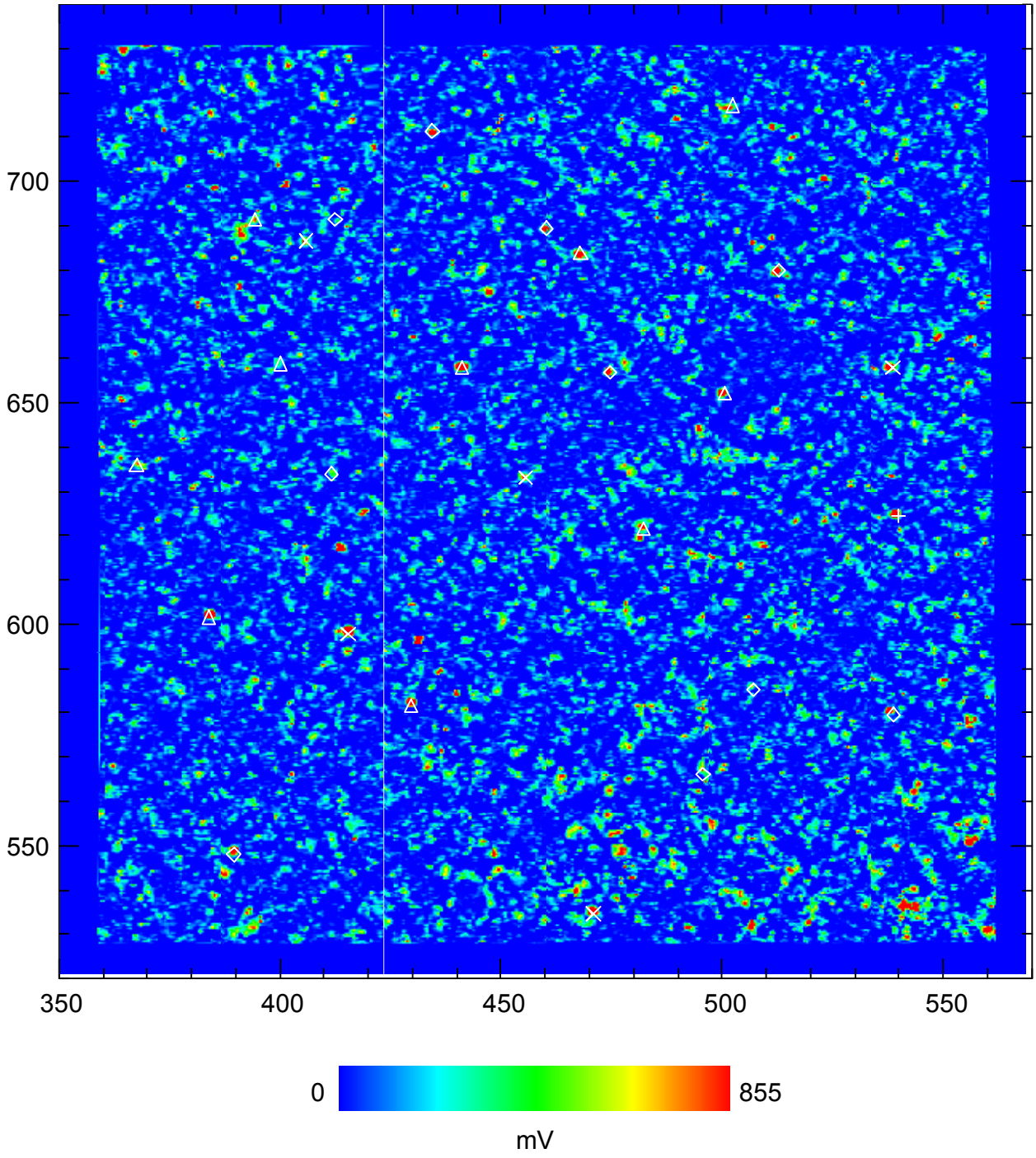

Figure 13 – EM61 MkII lower coil gate 3 anomaly image map of the Seeded Area at the BBR Impact Area. The projectile targets are marked, diamonds for 105-mm, triangles for 155-mm, X for 8-in, and + for the live 155-mm.

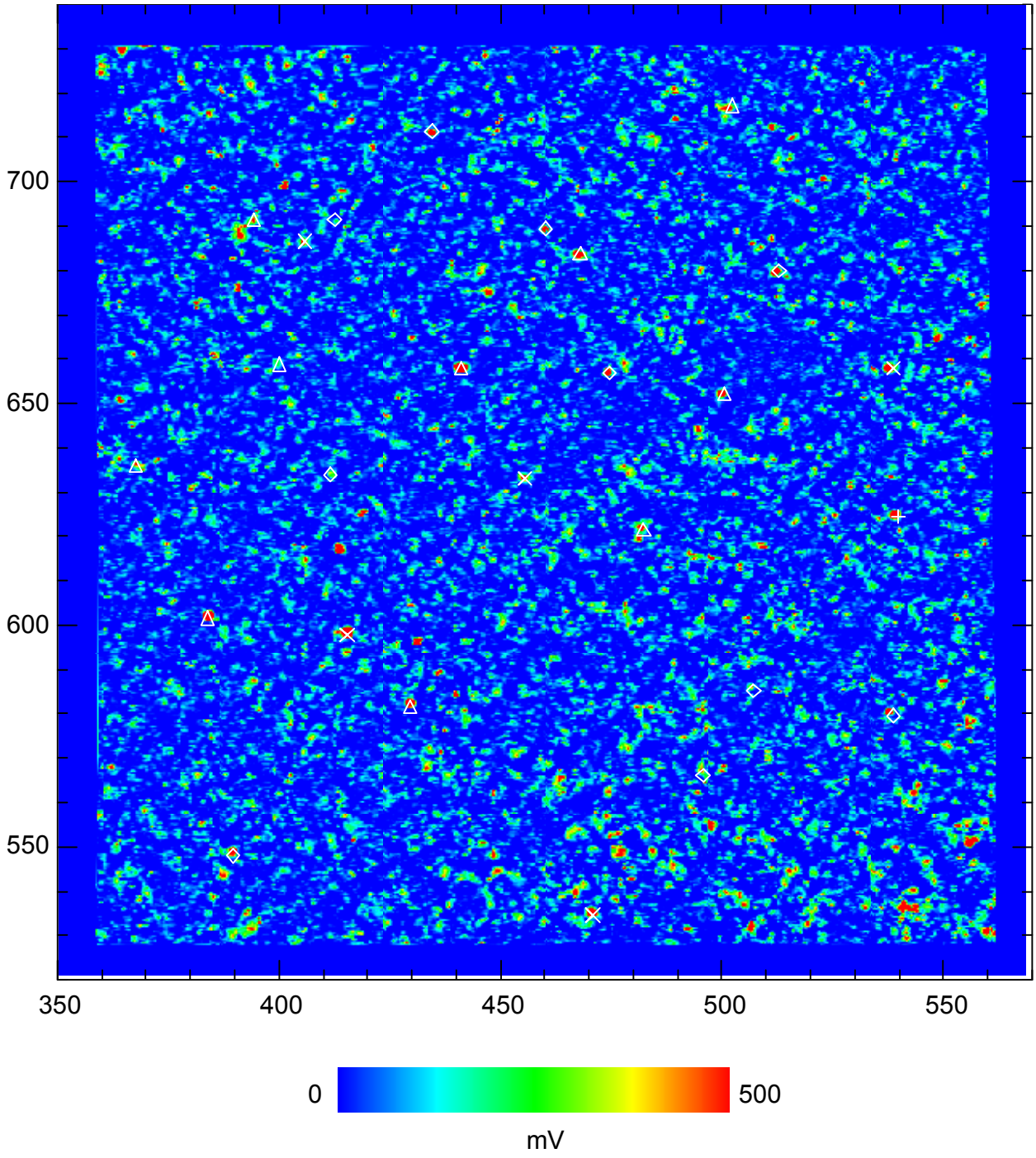

Figure 14 – EM61 MkII lower coil gate 4 anomaly image map of the Seeded Area at the BBR Impact Area. The projectile targets are marked, diamonds for 105-mm, triangles for 155-mm, X for 8-in, and + for the live 155-mm.

5.1.2.3 EM61 MkI Measurements Two orthogonal EM61 MkI surveys were also conducted as part of this Demonstration. An anomaly image map of the N/S survey is shown in Figure 15.

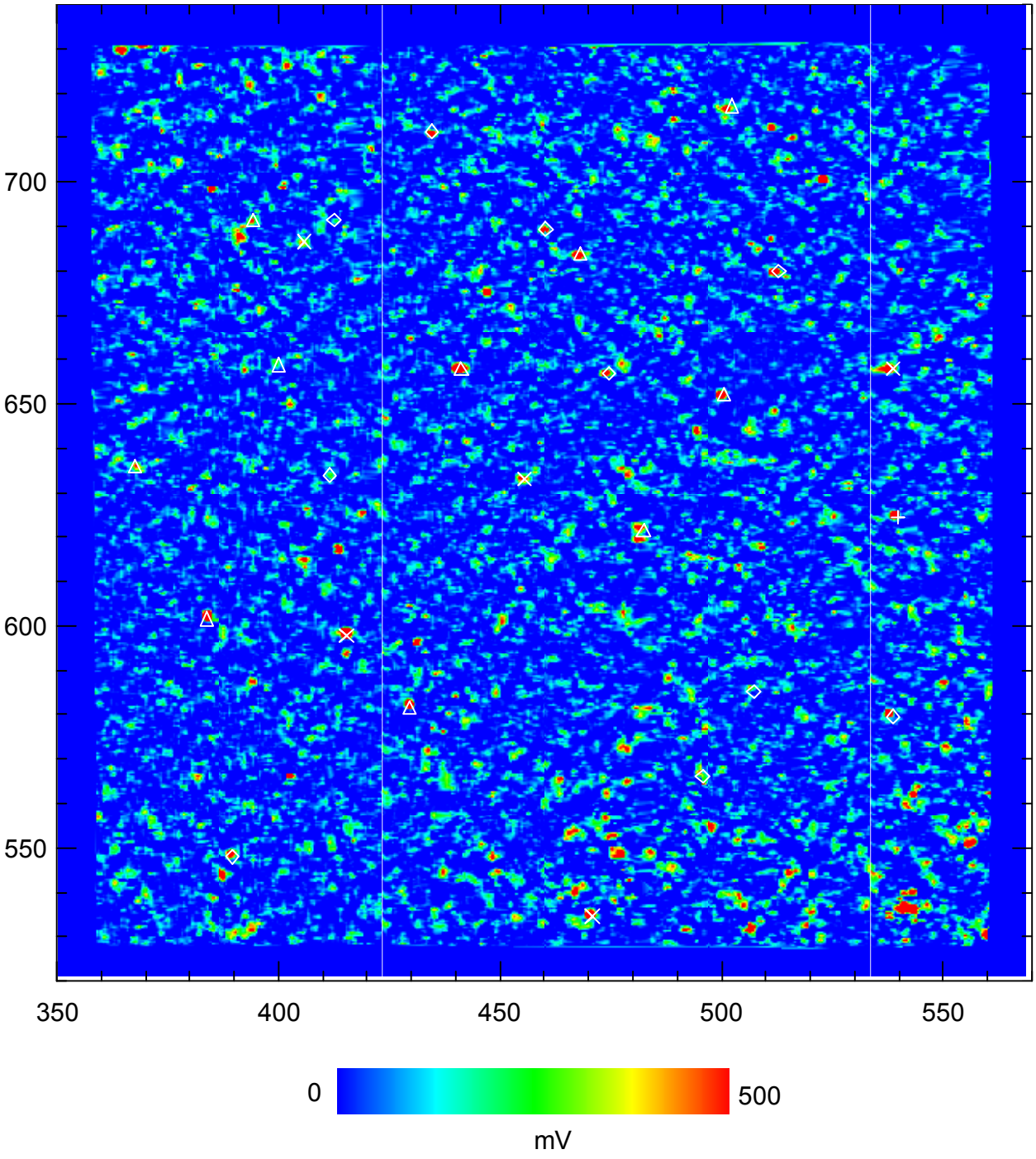

Figure 15 – EM61 MkI upper coil anomaly image map of the Seeded Area at the BBR Impact Area. The projectile targets are marked, diamonds for 105-mm, triangles for 155-mm, X for 8-in, and + for the live 155-mm.

A comparison of the results of the three surveys is shown for a small region of the Seeded Area in Figure 16. The same labeling scheme for the targets is used as in the previous figures.

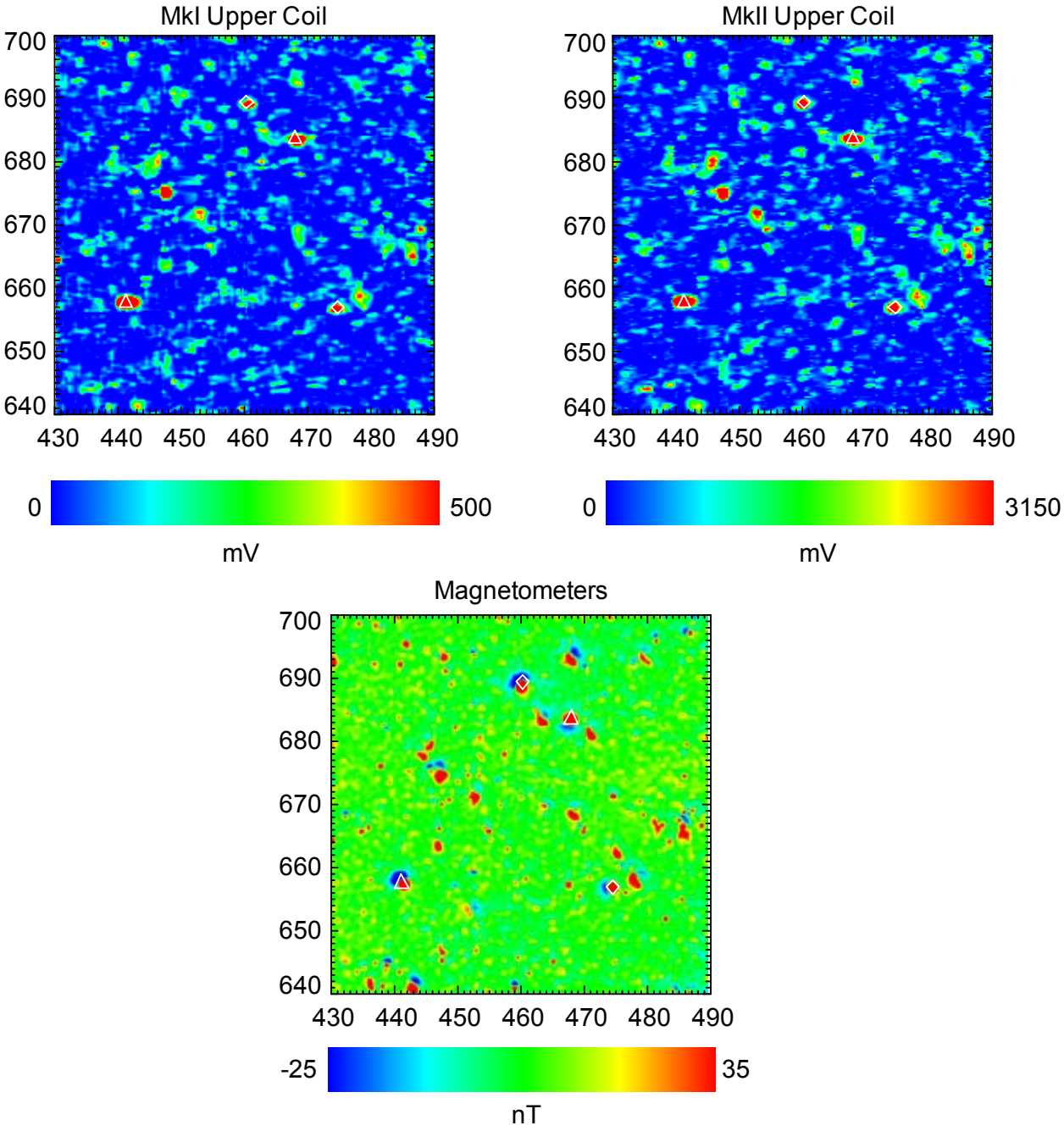

Figure 16 – Comparison of the results from all three surveys of the Seeded Area in a small subgrid

5.2 Data Assessment

5.2.1 EM61 MkII

5.2.1.1 Signal-to-Noise Ratios The first observation one makes about the EM61 MkII data is the relatively low S/N ratios at this site. Figure 17 compares a noise raster for the four MkII gates at the Badlands Site to the corresponding raster from the Blossom Point Test Site. Figure 18 is a power spectral density plot of the data from a larger raster.

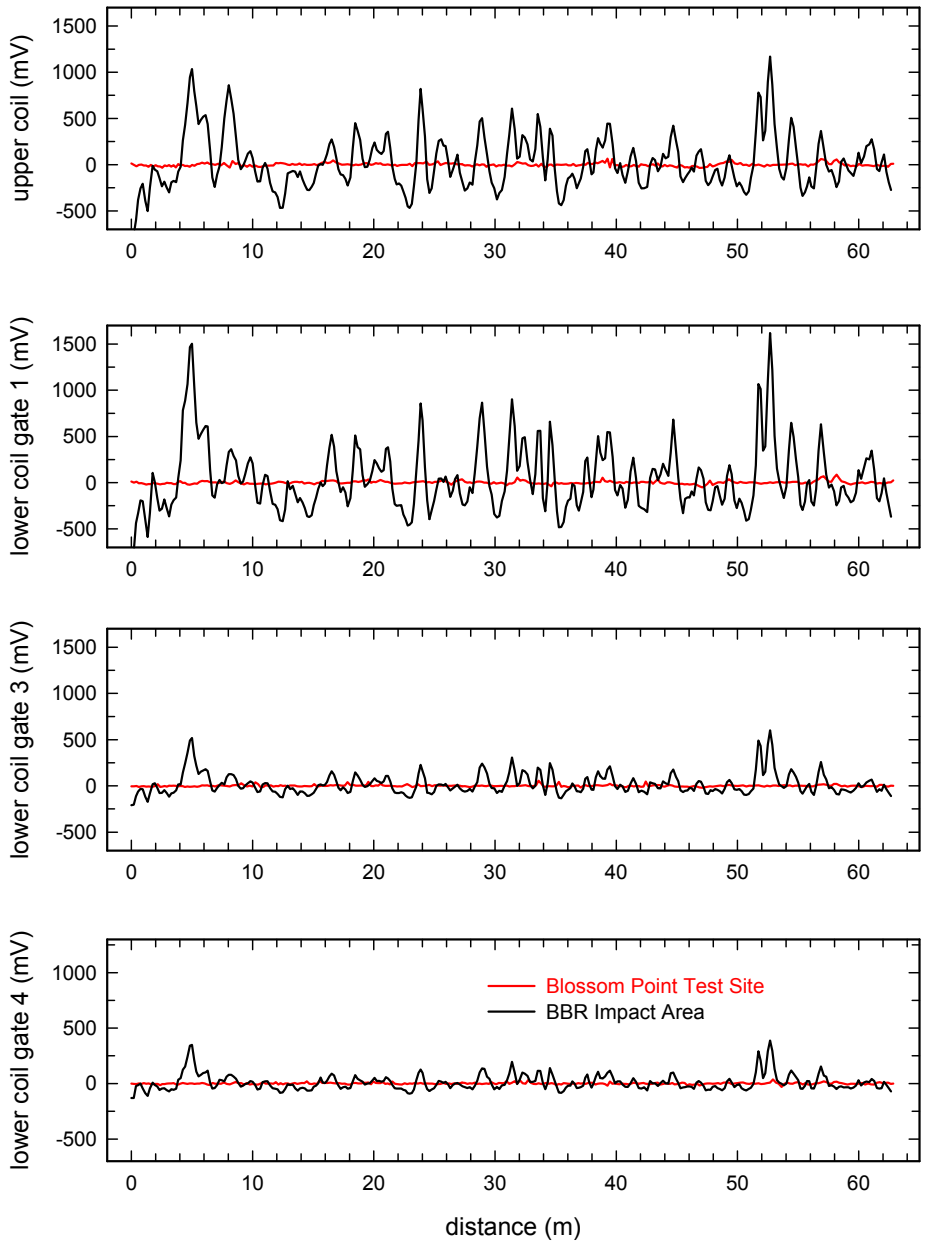

Figure 17 – Comparison of the noise measured in each of the EM61 MkII gates at the Badlands Bombing Range Impact Area with that measured at the Blossom Point Test Site

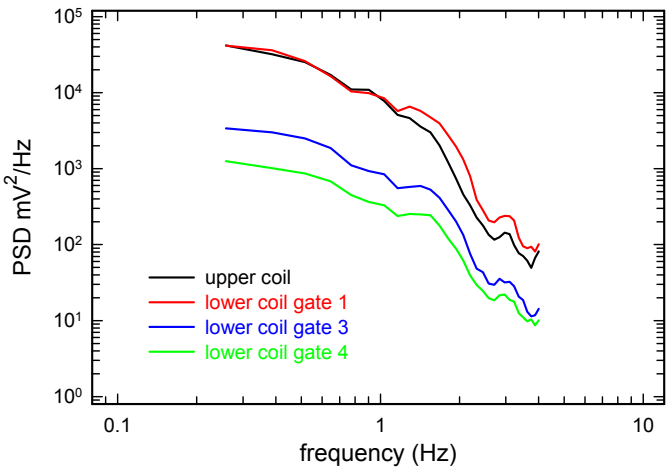

Figure 18 – Power spectral density of the EM61 MkII noise measured at the Badlands Bombing Range Impact Area

From Figure 17, one can see that the noise, defined here as the sum of sensor noise (primarily uncorrelated among the gates) and the signal due to non-UXO targets (correlated among the gates), is substantially higher at the Impact Area than at the Blossom Point Test Site. This is to be expected given the high density of small frag and clutter that litters the Impact Area. Even given this, the measured noise (1000 mV in some cases) is very large and, as will be seen below, seriously interferes with our ability to achieve a reliable model fit to the survey data. The PSD of the four channels tracks well. The plots exhibit broad peaks near 1 Hz and at 3 Hz. Both of these are presumably due to platform motion and will be discussed further below.

5.2.1.2 Electronic and Calibration Issues During initial examination of the MkII survey data we discovered several other features that compromised our ability to achieve reliable model fits. Between time gates on a single MkII and among the three MkII sensors in the array, discrepancies were found in the gain factors, the sampling times, and the noise levels.

The MkII sensor measures the current in the transmit coil and uses this to normalize the output signal. This is done to maintain a constant output from the sensor as the battery voltage drops. When hooked up as an array of three sensors, one MkII is the master unit, and it triggers the two slave units. We initially noticed that the two slave sensors reported an odd oscillation of their transmit currents. Correcting the signal by these current variations caused their apparent signals to oscillate. Independent measurement of the transmit currents did not confirm these oscillations. In an array mode, the MkII sensors appear to have an electronic problem that causes an error in their current measurement circuitry. To correct for this, the current in the master sensor was used to normalize the signal in all three sensors. Even with this correction, problems were still observed with the relative outputs among the three sensors on the upper and lower coils and among the three time gates. A steel sphere was used as a calibration object to measure each sensors response and correction gain factors were found for each sensor and time gate. These correction factors were as large as 25% between sensors. Additionally, there was some indication that these factors may have been changing day to day as seen in the next section. The

MkI array was similarly calibrated, but had only minor corrections (10% between sensors) and appeared to be consistent from day to day.

The MkI array was originally tested for timing problems between sensors by driving back and forth over a long wire or pipe. Each sensor was found to have a fixed timing offset needed to correctly map the data. Over time, these corrections have never been observed to vary. The same test with the MkIIs found similar timing offsets, but the offsets were found to vary from data file to data file. To correct for this, a "wire test" was performed in the field for each data file collected, and offsets were found for each file. Despite this added correction, there were still stretches of data collected where varying timing offsets were observed. The only conclusion is that the timing offsets change within a data file. Since the time of this Demonstration, this sensor timing variation has been confirmed by other groups using the EM61 MkIIs.

Finally, from data file to data file and day to day, the noise levels on certain sensors and certain time gates has been observed to change. At times, the noise was as much as five times greater. This noise dominated short time scales and was present even when the sensors were stationary. An example of this sample-to-sample jaggedness is shown in the next section.

5.2.1.3 Model Fits The implications of the electronic problems discussed above are illustrated in Figures 19 and 20. Figure 19, a comparison of the measured signal from the MkI and MkII arrays over target 142, shows excellent agreement between the two measurements. The MkII array data from target 13, in contrast, exhibits several of the electronic problems as illustrated in Figure 20. The large number of targets affected by these problems make the data from the EM61 MkII array suspect for classification purposes.

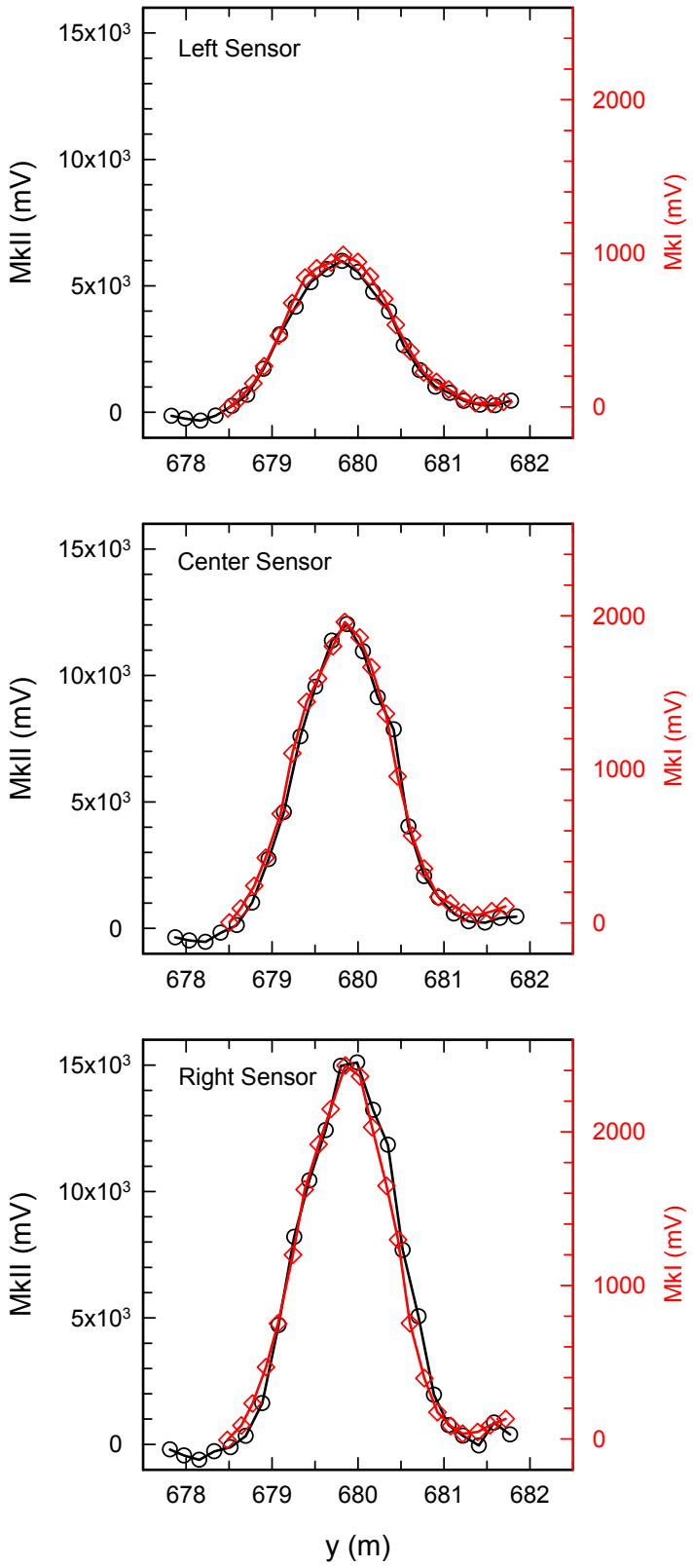

Figure 19 – Comparison of the signals from the MkII and MkI arrays over target 142

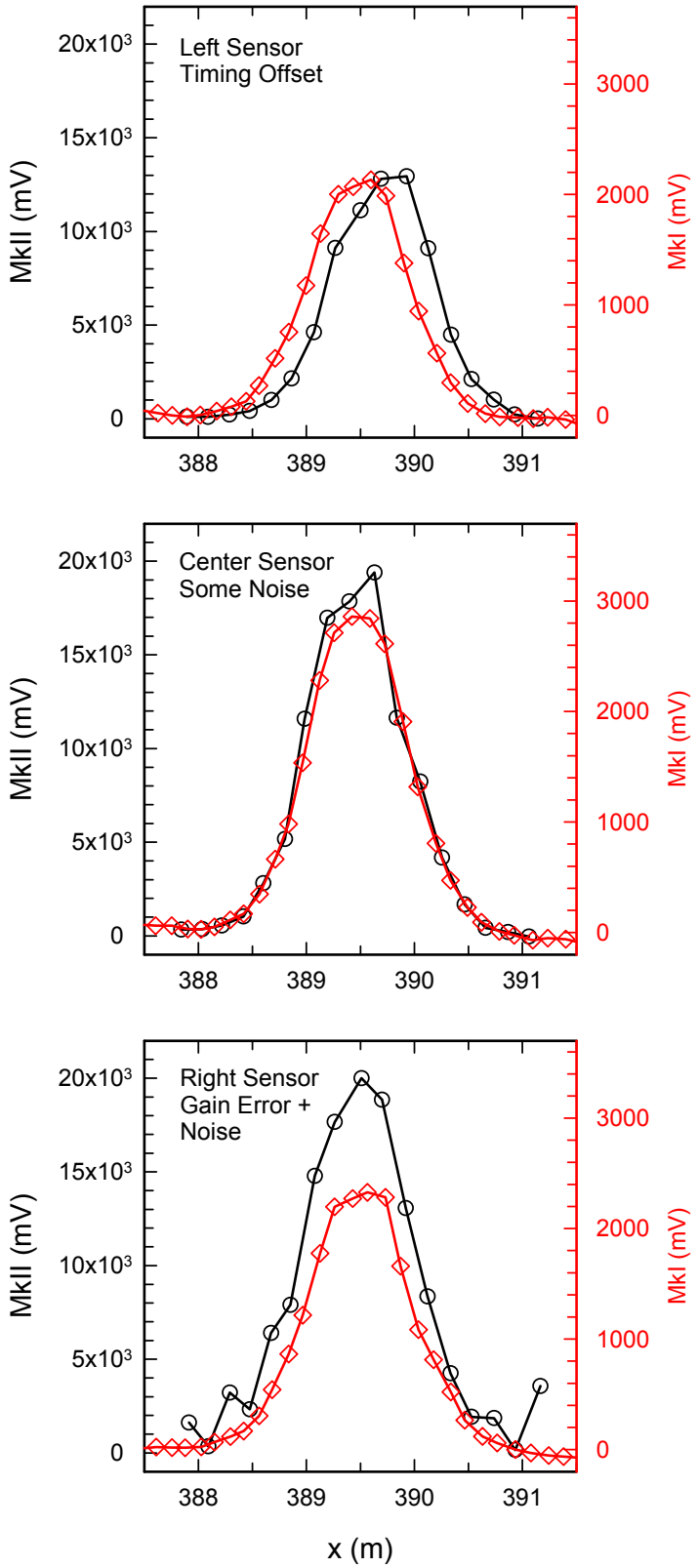

Figure 20 – Comparison of the signals from the MkII and MkI arrays over target 13

5.2.1.4 Comparison to EM61 MkI Given the inconsistent and unpredictable performance of the EM61 MkII discussed above, we must ask if there is enough new information in this sensor to justify the difficulty in using it. Figures 21 and 22 show a comparison of the data collected by the EM61 MkII with that collected by the EM61 MkI over a high- and low-SNR 105mm projectile respectively. In each of the figures, the upper coil signal is compared directly and the EM61 MkI lower coil signal is compared to all three lower-coil gates. Since the gain is higher in the EM61 MkII, the signals to be compared have been scaled to be the same at the peak signal over the object.

As can be seen most clearly in the high-SNR example, but is also evident in the low-SNR case, the signal in the later gates of the EM61 MkII is no different than that in the single lower coil gate in the EM61 MkI. Given the results presented in Figures 6 and 8, this result is not unexpected. It is clear that the EM61 MkII in the configuration used during this Demonstration does not add significant classification capability to the *MTADS* system.

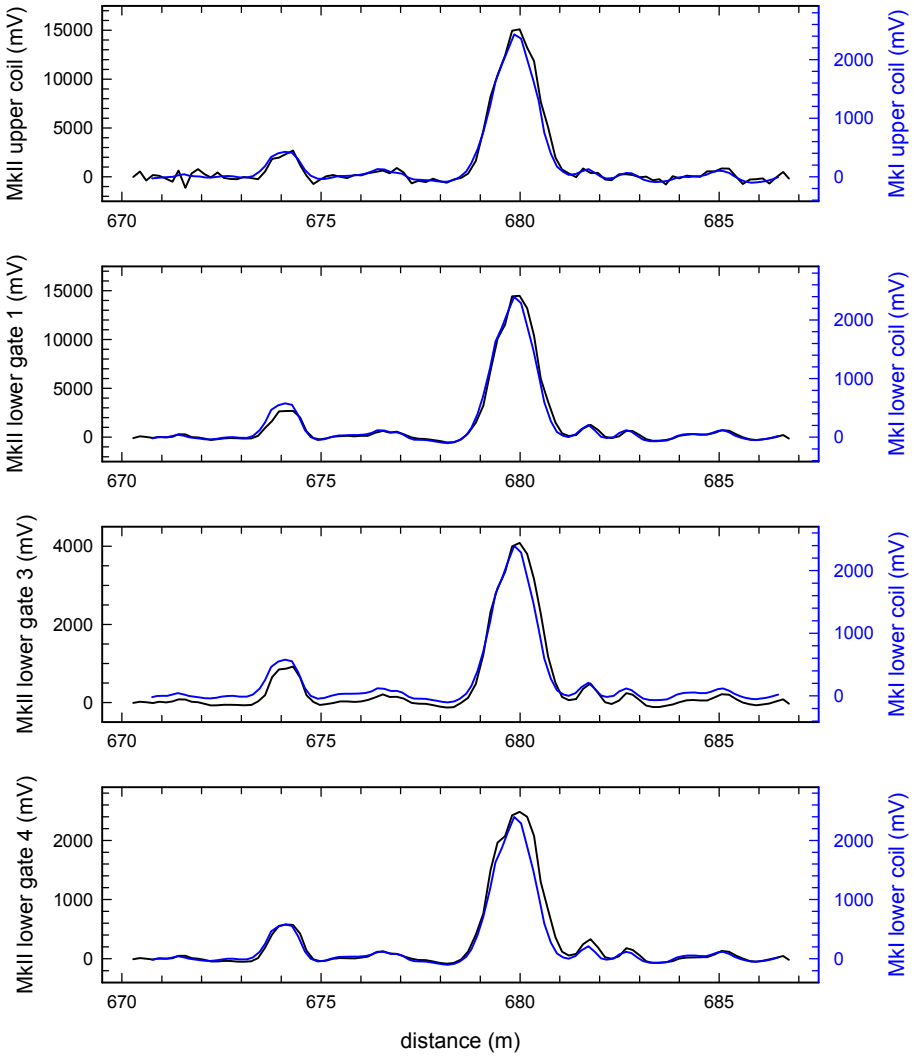

Figure 21 – Comparison of the signal from the EM61 MkII array (black) with that from the EM61 MkI array (blue) arising from a high-SNR 105mm projectile

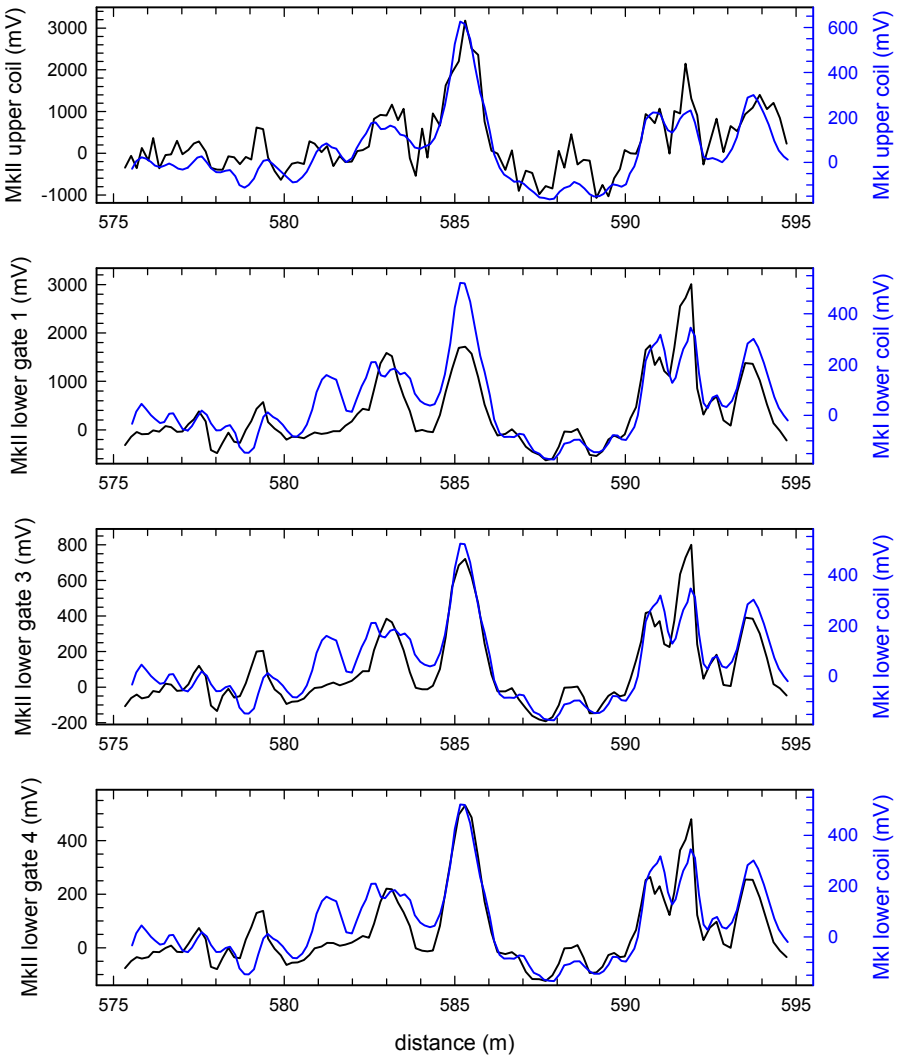

Figure 22 – Comparison of the signal from the EM61 MkII array (black) with that from the EM61 MkI array (blue) arising from a low-SNR 105mm projectile

5.2.2 EM61 MkI

5.2.2.1 Signal-to-Noise Ratios Three data rasters illustrating the relative noise levels at the Blossom Point Test Site, the Blossom Point "L" Range, and the Badlands Bombing Range Seed Area are shown in Figure 23. This plot confirms the relative noise levels seen with the MkII between the Blossom Point Test Site and the Badlands Bombing Range. Figure 24 is a power spectral density plot for the data from those two sites.

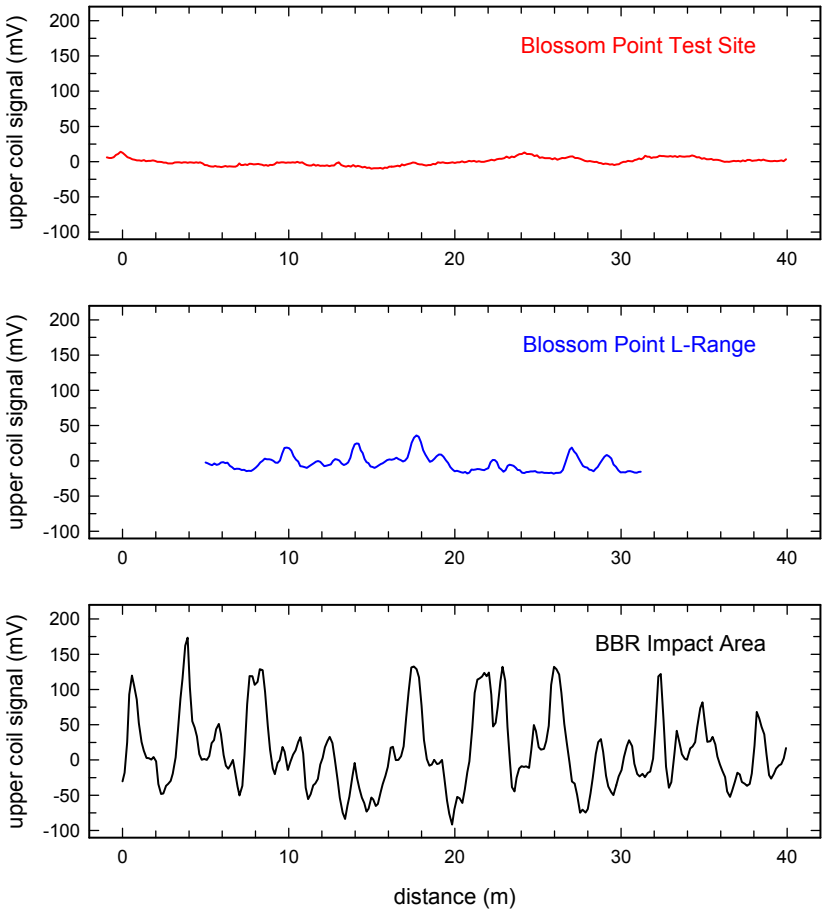

Figure 23 – Comparison of the noise observed with the EM61 MkI at three sites

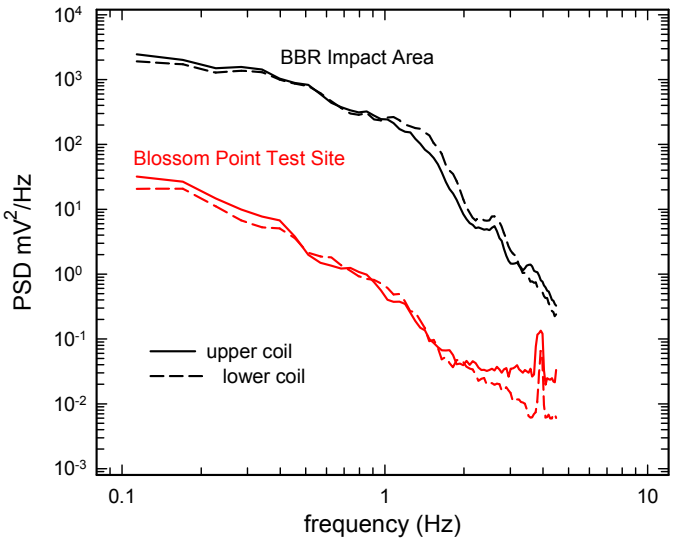

Figure 24 – Power spectral density of the EM61 MkI noise at two sites

5.2.2.2 Model Fits The original goal of this Demonstration was to invert the data over each anomaly and, using the beta response coefficients, to identify each ordnance item and discriminate the ordnance from the clutter. In all, 70 anomalies exhibited signal amplitudes at least twice the background. The peak EMI signatures ranged in amplitude from 400 to 9000 mV (arbitrary units from Geonics EM61). Background variation over the scale lengths of the anomalies (several meters) was on the order of 100-200 mV, which as was seen in Figure 24 is much greater than at other sites we have surveyed. Of the seeded ordnance, three 105-mm's and one 155-mm did not meet this S/N threshold. The missed 105-mm's were deeper than 0.5 m. The missed 155-mm was 0.85-m deep. The 8-in's ranged in depth from 0.3 m to 0.75 m. Of the 37 non-ordnance items analyzed, there were 19 clusters of exploded fragments, 12 individual pieces of shrapnel, and 6 pieces of scrap metal from the auto bodies used as targets. The results for all fits discussed in this Section are listed in Appendix C.

The primary versus secondary fitted beta values for ordnance (left panel) and non-ordnance (right panel) are shown in Figure 25. The symbols plot the primary beta value versus the average of the secondary values. The vertical line through each symbol indicates the maximum and minimum secondary beta values. Ideally, for ordnance, the secondary beta values should be equal. The plotted circles are centered on the expected values for the betas of a 105-mm (solid), a 155-mm (dotted), and an 8-in (dashed). The circles are of equal radius on the log-log plots and in the left panel of Figure 25 contain all of the fitted ordnance items with a high signal to noise (S/N). These are shown with black symbols (105-mm as diamonds, 155-mm as squares, and 8-inch as triangles). The red symbols in the left panel represent ordnance fits from low SNR data (peak signals less than 1000 mV). These beta fits are far from the expected values. In the right panel of Figure 25, the symbols are: green diamonds for fragment clusters, blue squares for single fragments, and pink triangles for scrap. The signals ranged in amplitude from 400 to 1000 mV for the clusters, 500 to 2000 mV for the singles, and 700 to 4000 mV for the scrap. It should be noted that none of the non-ordnance betas fall entirely within the high SNR ordnance spheres.

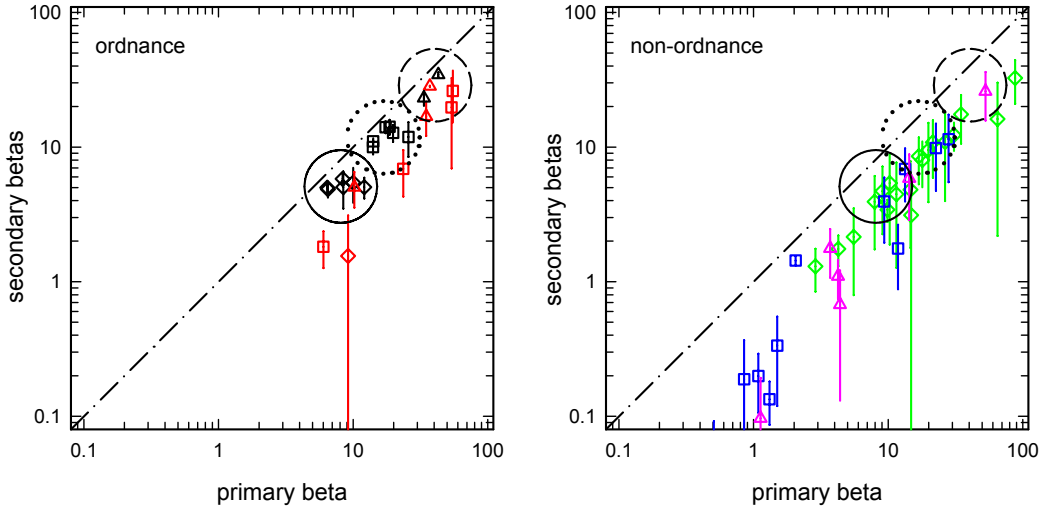

Figure 25 – Plots of primary beta vs. secondary betas for ordnance items (left panel) and clutter (right panel). Circles represent regions containing high-SNR fits of the three ordnance types. See the text for an explanation of the symbols.

In an effort to understand these low SNR fit results, both data/model fits and normalized chi-square surfaces for: a high SNR 155-mm, a low SNR 155-mm, and a fragment cluster are shown in Figures 26 – 28. The data rasters plot the measured data from the center sensor as it passes directly over the object. The black line is the data, the symbols are data used in the fit, and the colored lines represent the best model fit to the data. The chi-square surfaces are a function of primary beta value and depth below ground and have been normalized in each case to the minimum chi-square. In the high SNR case, Figure 26, the data and model fit very closely at a primary beta value of 14, and the curvature of the chi-square contours is very steep. For the low SNR case, Figure 27, the curvature is not as steep indicating a larger uncertainty in the fitted model parameters. Indeed, two model fits are shown in Figure 27: one at the minimum chi-square (red plots) with a beta value of 6.3 and one at a primary beta value of 14 (green plots). The differences between these two fits and the data are comparable to the signal variation due to noise. A major factor in these poor inversions is the simple EMI signal shape from large ordnance. Because of the small ratio of primary to secondary beta for large ordnance (~1.3), the signals are a simple single peak response and large variations in depth and primary beta produce very similar signal shapes.

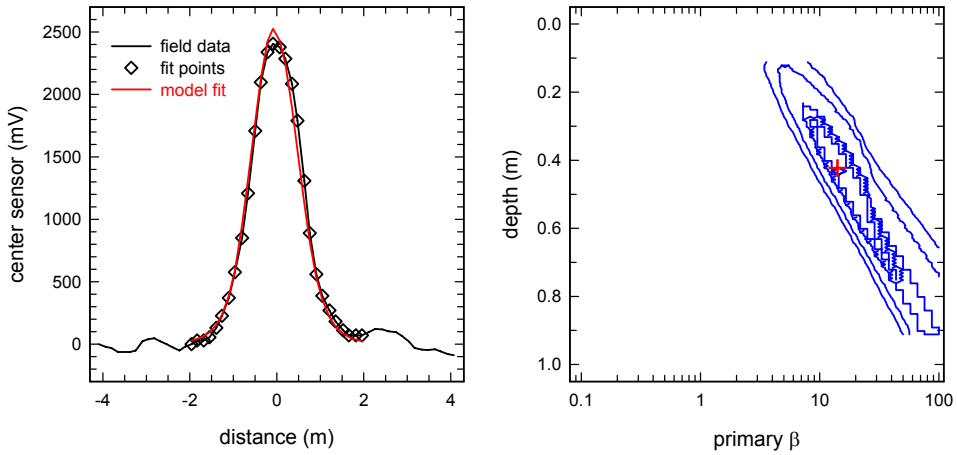

Figure 26 – Data fit and χ^2 contours for a high-SNR 155-mm projectile

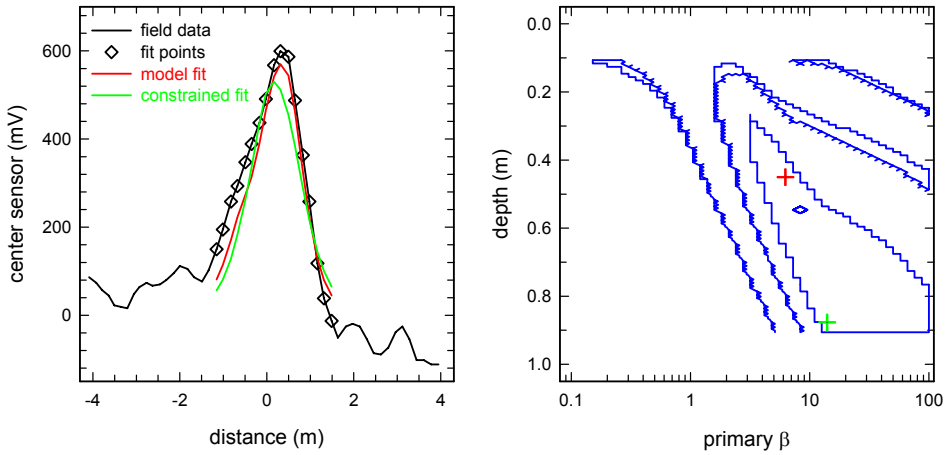

Figure 27 – Data fit and χ^2 contours for a low-SNR 155-mm projectile

Fragment clusters on the other hand, as shown in Figure 28, produce a broader merged two peak structure and typically show these features in any survey direction. This constrains the model to two large horizontal betas and a small vertical beta ($\beta_x = \beta_y > \beta_z$). These are the betas expected from a flat axisymmetric plate.[19] For this cluster, the betas were 12.5, 10.0, and 1.8. Even at low SNR, this two-peak structure remains significant, and the large spread in the secondary betas for all clusters can be seen in Figure 25. The normalized chi-square contours for this cluster are shown in the right panel of Figure 28. The curvature is not steep and the minimum is not well localized. This appears to be a result of the measured data simply not matching the model well no matter what the model parameters are. This poor match is not unexpected given that the signal comes from the sum of a number of small objects spread out over an area and not a single distinct metal object which is what the model is based on.

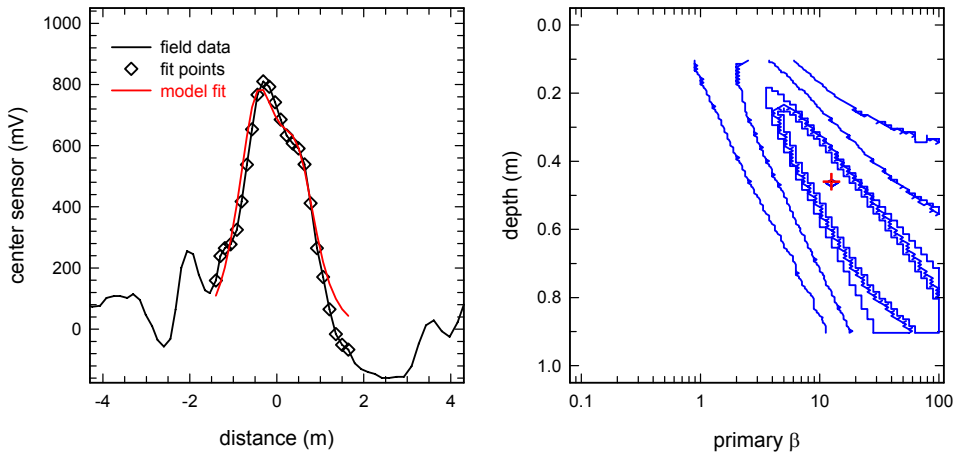

Figure 28 – Data fits and χ^2 contours for a frag cluster

5.2.2.3 An Alternate Discrimination Approach The consistent poor match between data and model for non-ordnance fragment clusters suggests using a goodness-of-fit metric as a means of discriminating between ordnance and clutter. After considering several, the reduced chi-square was found to be an effective discriminant. For each fit, this quantity was calculated as the sum of the difference between model and data squared divided by the standard deviation of the noise squared and divided by the number of degrees of freedom. The noise was assumed to be roughly gaussian with a standard deviation of 100 mV. Simple distributions of the background showed this only to be approximately true. The reduced chi-square as a function of peak signal for ordnance (left panel) and non-ordnance (right panel) is plotted in Figure 29. The colors and symbols denote the same items as in Fig. 25. The dotted line denotes a straightforward means of discrimination by considering the ratio of the reduced chi-square to the peak signal.

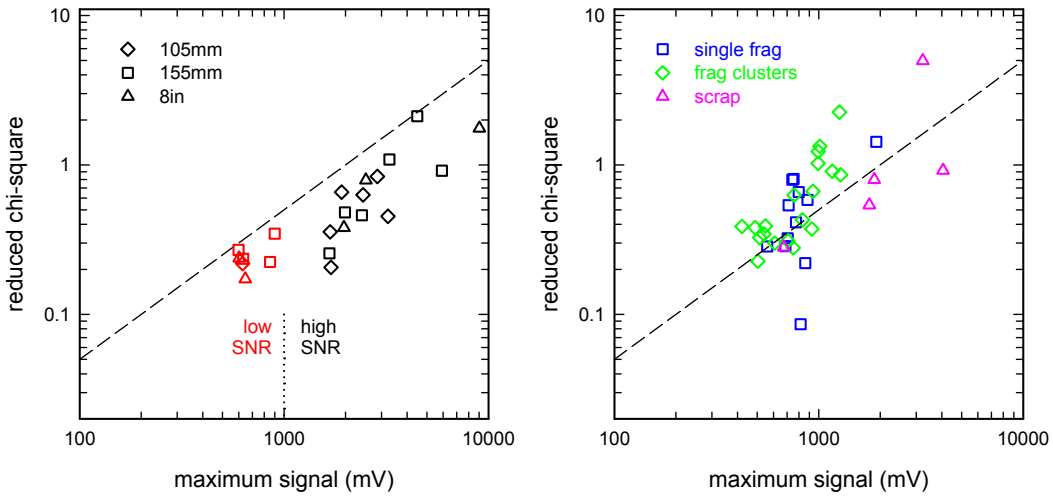

Figure 29 – Plots of reduced chi-square vs. peak signal for ordnance (left panel) and clutter (right panel). The dashed line scales linearly with signal and indicates a rough threshold to separate ordnance from clutter. The symbols are the same as Figure 25.

The "beta sphere" method of discrimination is compared to this "goodness-of-fit" method in Figure 30. For the "beta sphere" approach, the three dimensional distance of the logarithm of the three fitted betas from the expected logarithm of the betas for the three ordnance items is calculated, and the minimum distance is kept for each. This beta distance is plotted as a function of object type in the upper panel of Figure 30, and again, the colors and symbols are the same as in Figure 25. Note, except for an 8-inch target that fit very close to the expected 105-mm betas, that all of the low SNR ordnance values are anomalously large and all of the high SNR values are reasonably distinct from the clutter. In the lower panel of Figure 30, the reduced chi-square divided by the peak signal is plotted as a function of object type. At a level that picks up all of the ordnance, this chi-square quantity only picks up a modest number of non-ordnance. This is quite an improvement over the "beta sphere" method in separating ordnance from clutter.

A further improvement on this discrimination was found by constraining the beta fits to the expected beta values for each ordnance type. Each target was fitted with the beta values for: a 105-mm (8.8, 5.1, 5.1), a 155-mm (16.8, 11.8, 11.8), and an 8-inch (40.6, 28.8, 28.8). The fit with the lowest chi-square was kept. The resulting primary beta as a function of target type is plotted in the upper panel of Figure 31. Curiously, actual 105-mm's fit equally to 105-mm betas and 155-mm betas; the 155-mm's fit to all three betas; the 8-inches fit to 155-mm and 8-inch betas. The clutter fits almost equally to all three ordnance betas. In the lower panel of Figure 31, the reduced chi-square from the constrained fitting is divided by peak signal and plotted as a function of object type. For this discriminant, all of the ordnance can be separated from all but four of the clutter items.

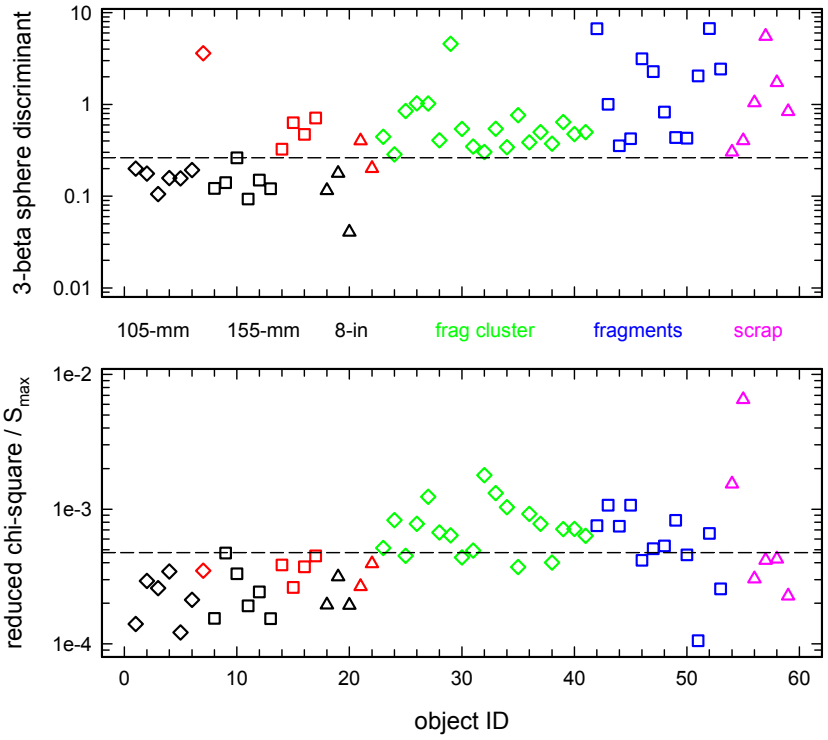

Figure 30 – Comparison of the "beta sphere" discriminant to the "goodness of fit" discriminant

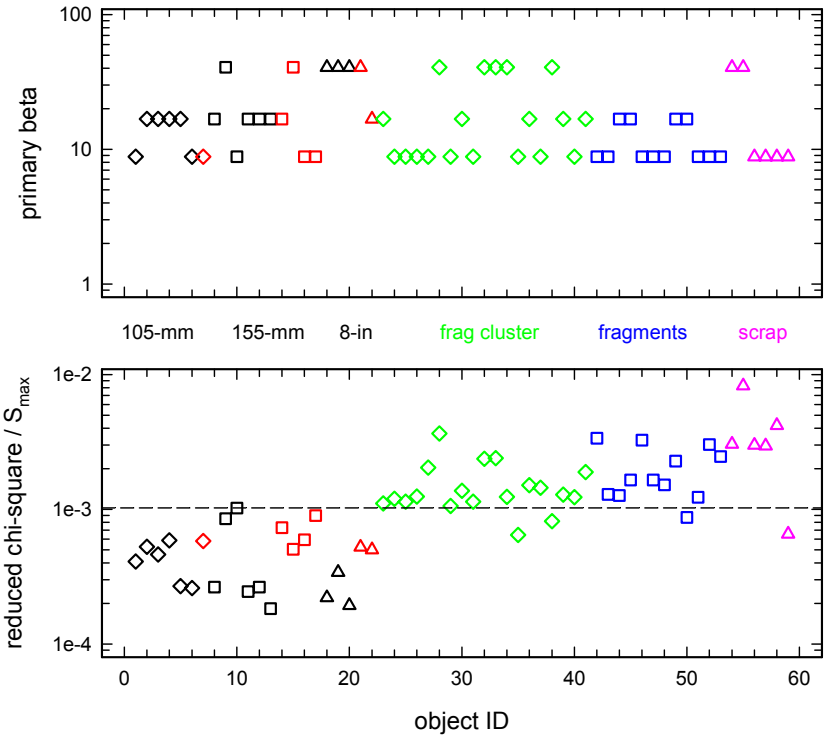

Figure 31 – Results of the constrained fits discussed in the text

The ROC curves in Figure 32 compare the relative performance of these three methods. As the three discriminant levels are varied, the number of ordnance items correctly identified as ordnance ("probability of detection") is plotted against the number of non-ordnance items incorrectly identified as ordnance ("probability of false alarm"). The "goodness-of-fit" discriminant based on the constrained beta fits provides the best overall performance.

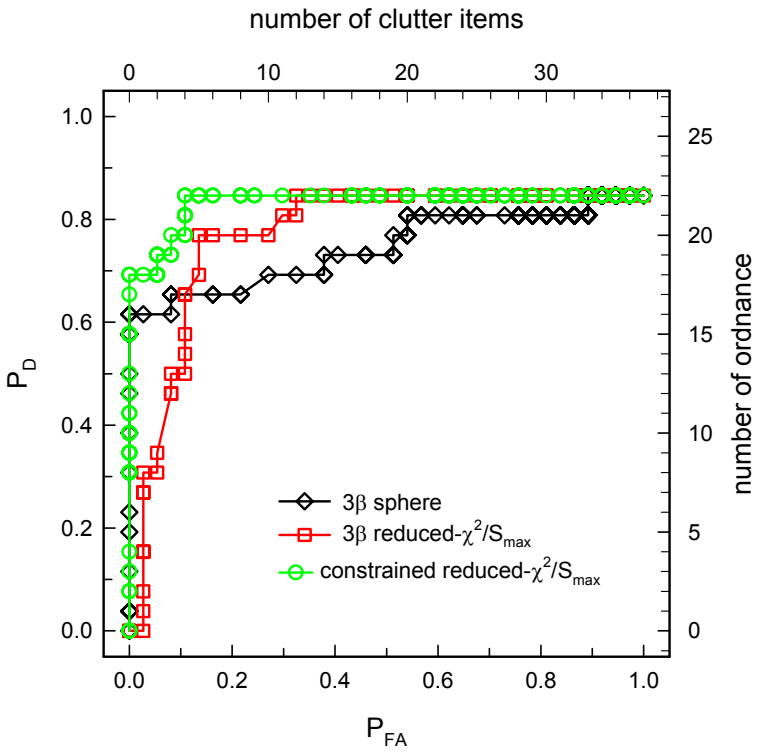

Figure 32 – ROC curves comparing the discrimination performance of the three methods discussed in the text

5.3 Platform Motion

We have shown previously that, as is intuitively obvious, the quality of our model fits, and thus our classification ability is directly proportional to the accuracy with which we can locate individual sensor readings in x, y, and z.[14] Previous Demonstrations of this technology used a single GPS antenna, labeled GPS1 in Figure 33, to provide position. There is an approximately 1.5-m offset from this antenna to the center of the sensor coil to avoid electronic interference. Sensor locations were calculated by projecting back from the GPS antenna along a track derived from successive GPS readings. Obviously, any deviation in this track resulting from GPS noise is amplified in this projection. Our previous work has demonstrated that we need to locate the sensors with cm-level precision for useful model fits. This location precision is not possible with our original technique.

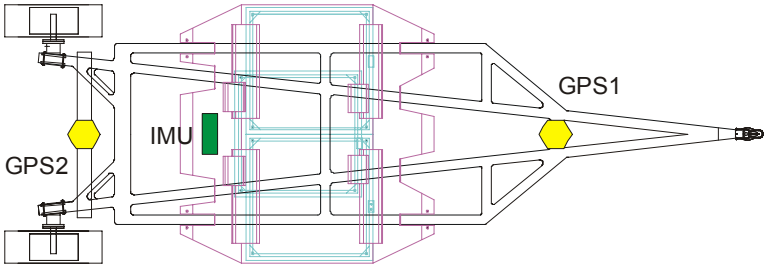

Figure 33 – Bird's-eye view of the *MTADS* EMI sensor trailer showing the relative locations of the two GPS antennas and the IMU

For this Demonstration, we modified our location system in two ways. First, we added another GPS antenna on the centerline of the sensor trailer behind the sensors. The two GPS receivers (Trimble Navigation Ltd., model MS750) work cooperatively to report absolute position and the vector between the two antennas at 5 Hz. This upgrade removes much of the track noise we have experienced in prior Demonstrations. We have also shown that sensor orientation relative to the ground is an important variable in our model fits. The two-GPS system shown in Figure 33 provides pitch of the sensor trailer but, since the two antennas are on the centerline, is unable to provide any information about platform roll. To measure this variable, we employed a commercial 6 degree-of-freedom inertial measurement unit (IMU) (Crossbow, VG600CA) to obtain accelerations and angles of the sensor platform. As shown in Figure 33, the IMU was mounted on the rear of the tray that contains the EM61 coils. For this Demonstration, we polled the IMU at 20 Hz although the instrument has the bandwidth to reach 100 Hz.

When we first deployed the IMU system at Blossom Point, we immediately learned something about platform modes. Figure 34 shows a plot of vertical acceleration of the platform under

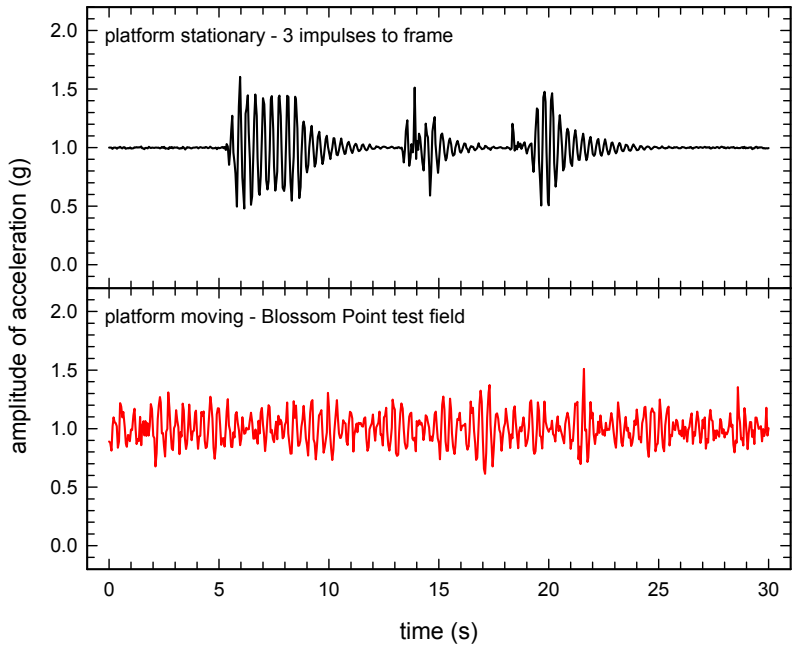

Figure 34 – Measured vertical acceleration of the EMI platform under static and moving conditions

static and moving conditions. Inspection of these two plots reveals a dominant mode common to the two conditions. This is shown more clearly in Figure 35 which shows a power spectral density plot of the two data sets. There is a clear mode at approximately 3 Hz and a smaller one near 7 Hz. A cartoon of the motion corresponding to this platform mode is presented in Figure 36. Obviously, this motion will modulate the sensor response over a target and thus must be measured as precisely as possible.

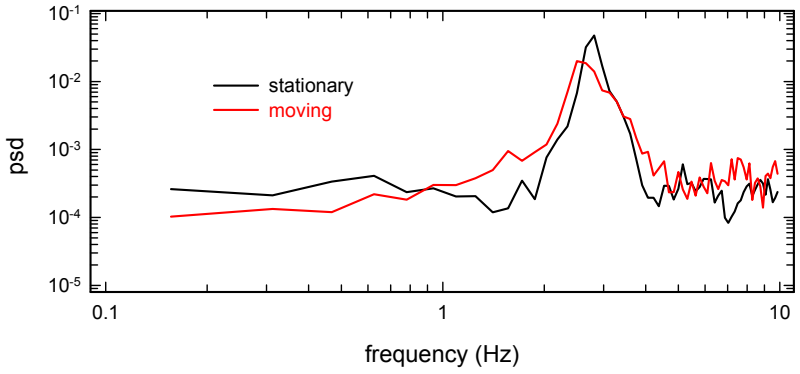

Figure 35 – Plot of power spectral density of the acceleration data from Figure 34 for the two cases

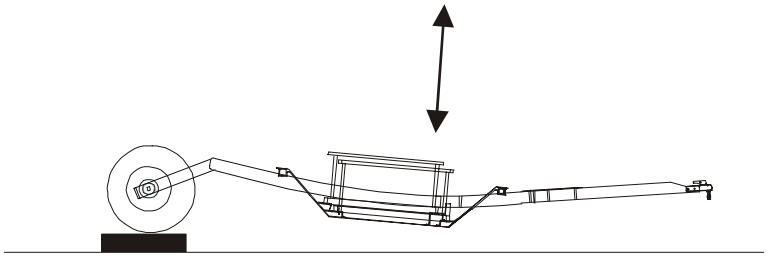

Figure 36 – Cartoon of the platform motion corresponding to the mode discussed in the text

5.3.1 Platform Motion During Surveys

The measured platform motion during a survey at the Blossom Point Test Site and the Impact Area is shown in Figures 37 and 38 respectively. In each case the data are from a N-S survey line. The top panel shows the progress up the line as recorded by the GPS. The second panel records the z-variation as measured by the GPS. The lower two panels plot platform motion; panel three plots pitch as recorded by both the GPS and IMU although the sign of the motion is reversed for the two sensors and the bottom panel plots platform roll.

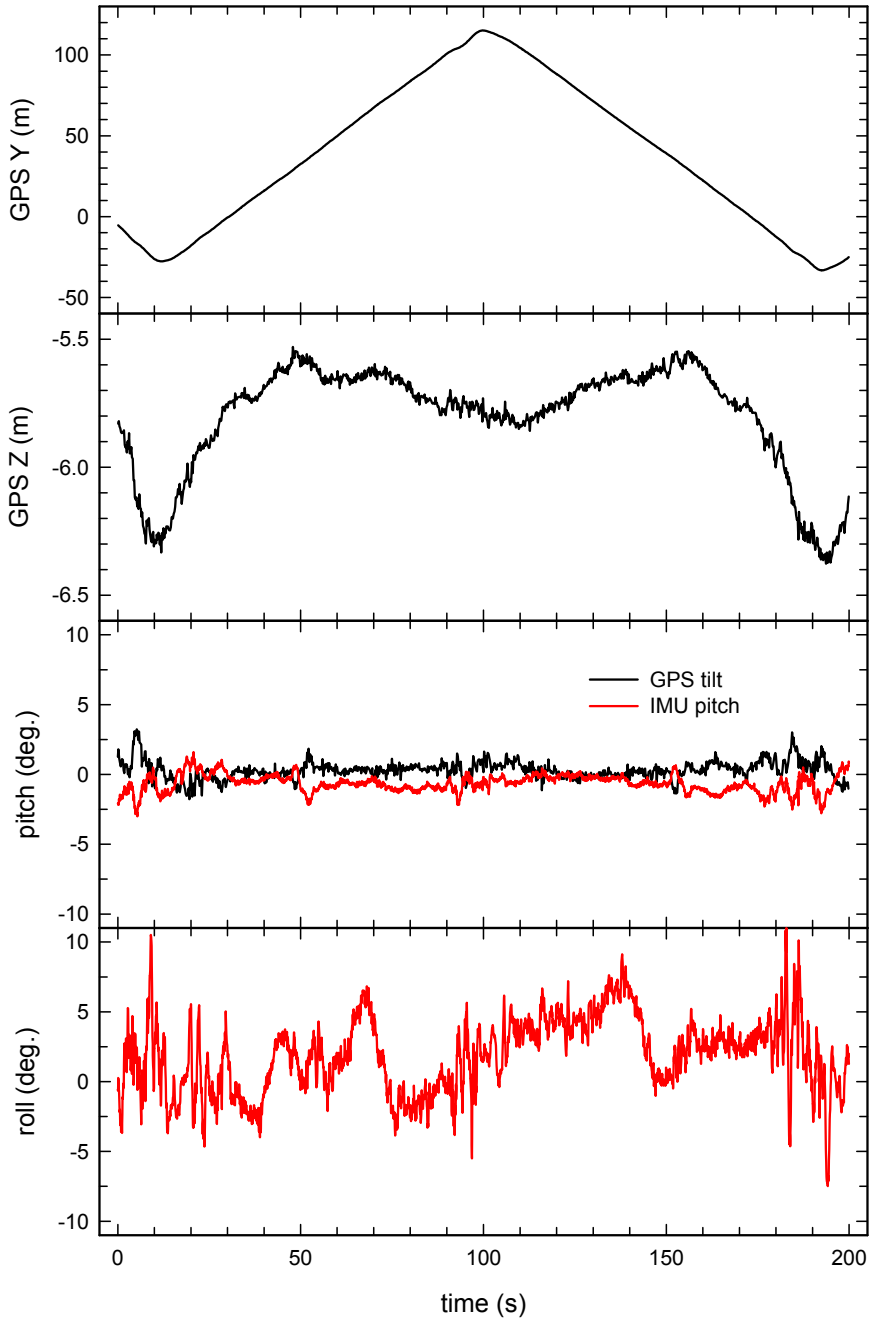

Figure 37 – Measured platform motion during a N-S survey at the Blossom Point Test Site. The top panel plots the progress up the line and the next panel plots the height variation, both measured by GPS. The third panel plots the platform pitch as measured by the GPS and IMU and the bottom panel plots platform roll.

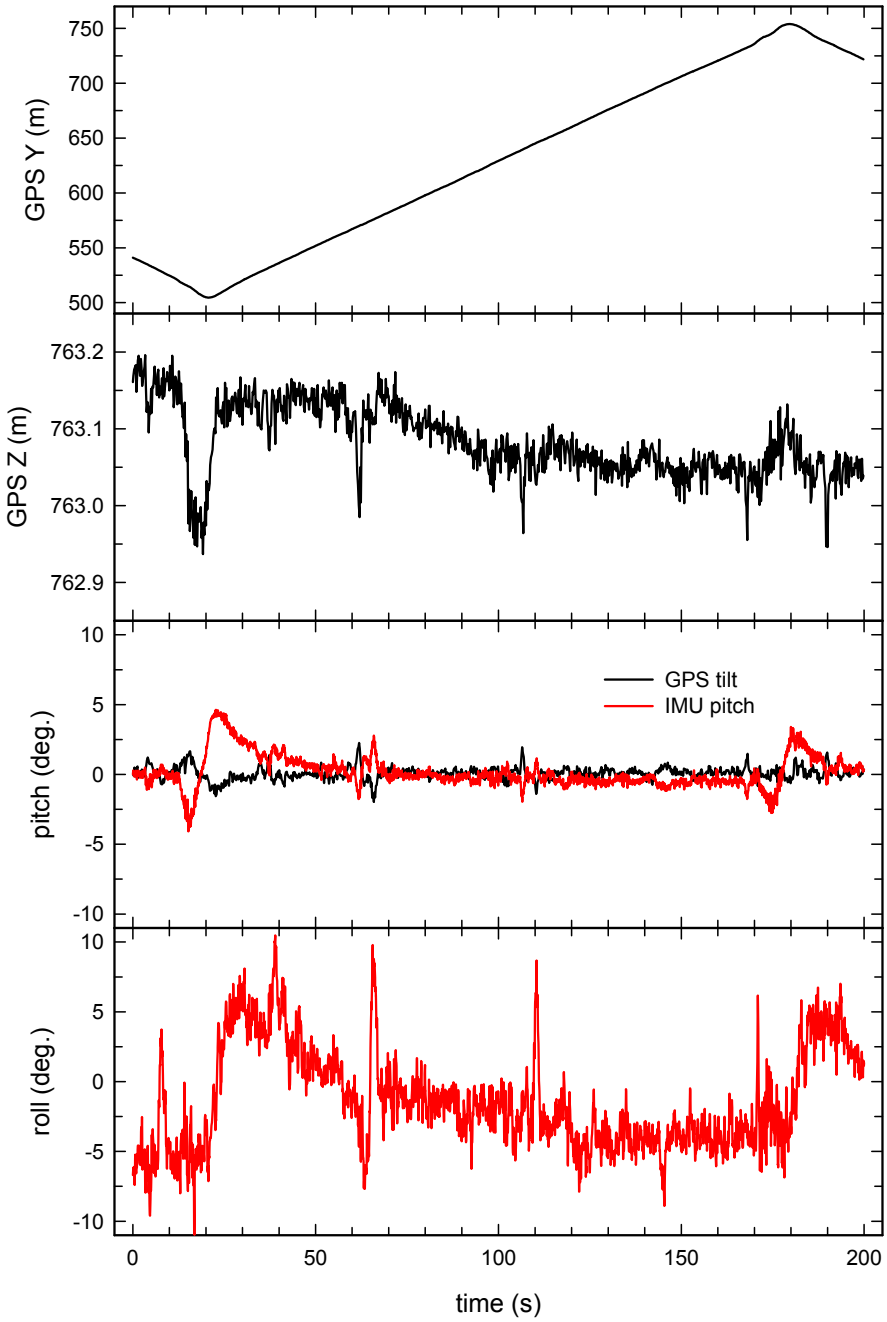

Figure 38 – Measured platform motion during a N-S survey at the Impact Area. The top panel plots the progress up the line and the next panel plots the height variation, both measured by GPS. The third panel plots the platform pitch as measured by the GPS and IMU and the bottom panel plots platform roll.

The cartoon in Figure 39 shows the relative arrangement of the sensors and gives the definitions of the angles reported in Figures 37 and 38. As can be seen from the figures, there is much more high-frequency vertical motion of the platform at the Impact Area. This reflects the much rougher ground at a live impact site that is filled with craters from projectile detonations. This is also evident in the few large pitch excursions at the Impact Area that result from the tow vehicle or platform wheels dropping to the bottom of a crater. Similar sharp excursions are evident in the roll motion. Based on these measurements, pitch of ±5° and roll of ±10° need to be accommodated in any data analysis scheme employed.

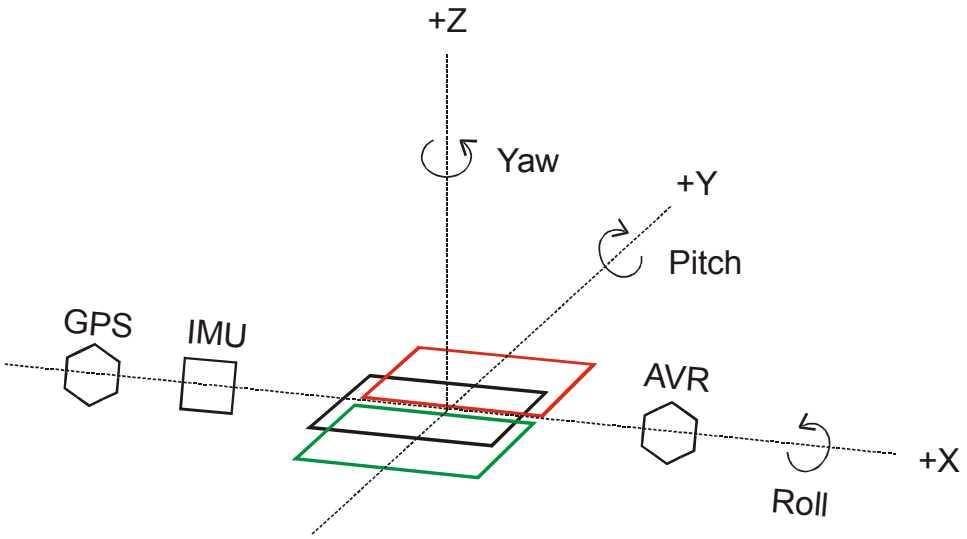

Figure 39 - Cartoon of the relative orientation of the platform motion sensors employed during this Demonstration and definition of the angles used in the text

This issue of platform motion is so important to the ultimate classification ability of a sensor array that we will implement a third GPS antenna to directly measure platform roll in future deployments of this system.

5.4 Technology Comparison

In Section 5.2 above, we have shown the results of our analysis of the EM results obtained during the Impact Area survey and demonstrated in Figure 32 that the normalized χ^2 from a constrained beta fit is the most effective discriminant. The baseline technology for comparison of these results is magnetometry. As mentioned in the Introduction, we have had considerable discrimination success when a skilled analyst fits magnetic anomalies and classifies the resulting targets. The magnetometry targets were categorized using the 6-bin priority (or confidence) scheme first introduced at JPG V and discussed above. The magnetometer data analysts attempted to scale their rankings such that digging all targets in categories 1-5 would clear all UXO from the site.[21] The model parameters resulting from the magnetometry analysis were also submitted to the PNN developed in the NRL/Blackhawk SERDP program. This neural net was trained using test pit measurements on the three ordnance types emplaced in the seed area.

Figure 40 shows a set of ROC curves comparing the performance of the constrained beta fit discriminant with those of the two magnetometry analyses. In contrast to Figure 32, the abscissa of this plot is false alarms per hectare. Since the two methods detected a different number of objects, this is the only way to make a meaningful comparison.

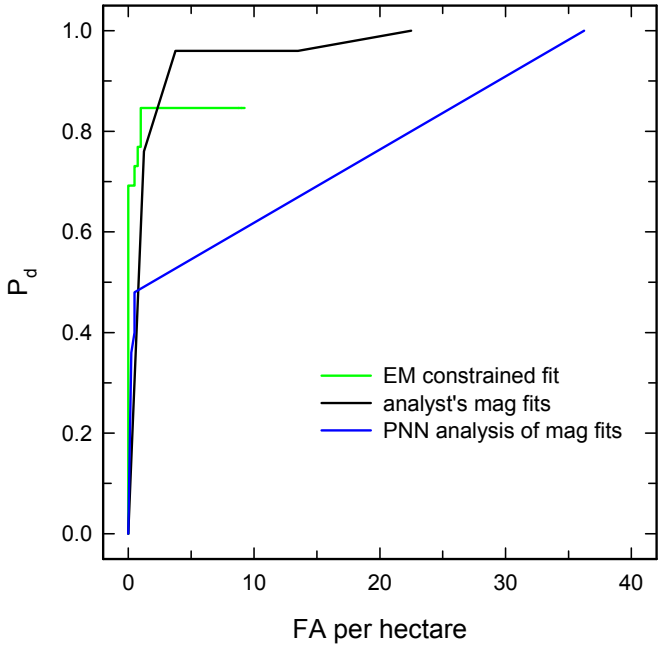

Figure 40 – ROC curves comparing the discrimination performance of the constrained beta fit discussed in the text with the two magnetometry analyses employed in this Demonstration

The most obvious point from Figure 40 is that the EMI system only detected 22 of the 26 ordnance items in the Seed Area. As discussed above, this is a function of the high noise in the EMI survey data. This noise arises from the near-saturation coverage of small frag pieces on this site to which the EMI system is much more sensitive. One obvious way to reduce this frag problem is to collect data at later times, after the contribution from the small frag pieces has decayed away. We discussed above the reasons this approach is not possible with the standard EM61 MkII that we deployed for this Demonstration.

6. Cost Assessment

The estimated costs for an *MTADS* EM survey in two directions and the data analysis required to implement the model described here for a hypothetical 200 acre survey are listed in Table 6.

Table 6. Estimated Costs for a Hypothetical 200-Acre Survey Using These Methods

Mobilization and Logistics		Survey and Analysis		Demobilization	
Activity	$K	Activity	$K	Activity	$K
Planning and Contracting	15	Surface Clearance	30	Site Cleanup	10
Equipment Transport	20	Field Surveys	150	Demobilization	10
Storage and Offices	5	Data Analysis	35		
Power and Fuel	5	Target Flagging	25		
Travel for Crew	5				
Miscellaneous	10				
Total	60	Total	240	Total	20

Note that the survey costs include two EM surveys only, no magnetometer survey is included. If large, deep targets were expected a magnetometer survey would be required and an additional $50K would be necessary. Since two perpendicular EM surveys are included in the estimate while only one would be required for target detection, it is clear that the added cost of these methods is $375 per acre. This is less than the cost required to remediate two targets per acre. Thus, the economic breakeven point for the use of these methods is reached when two false alarms per acre are avoided.

7. Lessons Learned

There are two primary take-away lessons from this Demonstration. At a live site like this, with heavy coverage of small frag and clutter, time-domain EMI methods are limited by the high noise at early times. The obvious solution to this is to record the signal later in the decay; this brings a host of problems that are under active investigation in several SERDP and ESTCP programs. Second, measurement, or control, of sensor platform motion is vital if one hopes to achieve good classification performance. We have demonstrated many times the degradation in model fit reliability that accompanies large platform motion. We have begun to tackle this problem and will report on the value of a three-GPS/IMU system in a later report.

8. References

1. "Hand-held Gradiometer Survey Test at The Marine Corps Air Ground Combat Center, Twentynine Palms, CA," NAVEODTECHCEN TR, September 1992. This report describes hand-held gradiometer surveys of the MCAGCC Magnetic Test Range conducted by military EOD teams. Their ordnance detection efficiency varied between 25 and 35%.

2. "*MTADS* TECHEVAL Demonstration, October 1996," H. H. Nelson, J. R. McDonald, and Richard Robertson, NRL/PU/6110--97-348.

3. "Results of the *MTADS* Technology Demonstration #2, Magnetic Test Range, Marine Corps Air Ground Combat Center, Twentynine Palms, CA, December 1996," J. R. McDonald, H. H. Nelson, R. A. Jeffries, and Richard Robertson, NRL/PU/6110--97-349.

4. "Results of the *MTADS* Technology Demonstration #3, Jefferson Proving Ground, Madison, IN, January 13-24, 1997," H. H. Nelson, J. R. McDonald, R. A. Jeffries, and Richard Robertson, NRL/PU/6110--99-375.

5. "*MTADS* Unexploded Ordnance Operations at the Badlands Bombing Range, Pine Ridge Reservation, Cuny Table, SD, July 1997," J. R. McDonald, H. H. Nelson, J. Neece, Richard Robertson and R. A. Jeffries, NRL/PU/6110--98-353.

6. "*MTADS* Demonstration at the Former Ft. Pierce Amphibious Base, Vero Beach, FL, March 1998," J. R. McDonald, H. H. Nelson, R. A. Jeffries, Richard Robertson, and K. Blankinship, NRL/PU/6110--98-372.

7. "*MTADS* Live Site Survey, Bombing Target #2 at the Former Buckley Field, Arapahoe County, CO," J. R. McDonald, H. H. Nelson and R. Robertson, NRL/PU/6110--99-379.

8. "*MTADS* Geophysical Survey at The Jamaica Island and Topeka Pier Landfills at The Portsmouth Naval Shipyard, Kittery, ME, October 1998," J. R. McDonald, H. H. Nelson and B. Puc, NRL/PU/6110--99-381.

9. "*MTADS* Live Site Demonstration, Pueblo of Laguna, 6 July – 7 August 1998," J. R. McDonald, H. H. Nelson and R. A. Jeffries, NRL/PU/6110--00-398.

10. "*MTADS* UXO Survey and Remediation on the Walker River Paiute Reservation, Schurz, NV, November 1998," J. R. McDonald, H. H. Nelson, and R. A. Jeffries, NRL/PU/6110--00-406.

11. "*MTADS* Unexploded Ordnance Operations at the Badlands Bombing Range Air Force Retained Area, Pine Ridge Reservation, SD, September, 1999," J. R. McDonald, H. H. Nelson, R. Robertson, and R. A. Jeffries, NRL/PU/6110--00-424.

12. "*MTADS* Geophysical Survey of Potential Underground Storage Tank Sites at the Naval District Washington, Anacostia Annex," H. H. Nelson, J. R. McDonald, R. Robertson, and B. Puc, NRL/MR/6110--00-8435.

13. "Electromagnetic Induction and Magnetic Sensor Fusion for Enhanced UXO Target Classification," H. H. Nelson and Bruce Barrow, NRL/PU/6110--00-423.

14. ESTCP Cost and Performance Report. *Electromagnetic Induction and Magnetic Sensor Fusion for Enhanced UXO Target Classification.* http://www.estcp.org/documents/techdocs/199812.pdf

15. "Navy Tri-Service Environmental Quality Research Development, Test and Evaluation Strategic Plan," of October 1994, p. Cleanup - 21.

16. ESTCP Cost and Performance Report. *Multi-Sensor Towed Array Detection System*. September 1999. http://www.estcp.org/documents/techdocs/199526.pdf

17. "Collection and Analysis of Multi-sensor Ordnance Signatures with *MTADS*," Bruce Barrow and H. H. Nelson, *J. Environ. Engineering Geophysics*, **3**, 71 (1998).

18. "Model-Based Characterization of EM Induction Signatures for UXO/Clutter Discrimination Using the *MTADS* Platform," Bruce Barrow and H. H. Nelson, Proceedings of the UXO Forum 1999, Atlanta GA, May 25-27, 1999.

19. "Model-Based Characterization of EM Induction Signatures Obtained with the *MTADS* EM Array," Bruce Barrow and H. H. Nelson, *IEEE Trans. Geophys. Remote Sens.*, **39**, 1279 (2001).

20. "Preliminary Assessment/Site Inspection Report, Badlands Bombing Range-Impact Area;" Ellsworth AFB, SD; Draft-Final; U.S. Air Force Air Combat Command; Prepared for U.S. Army Corps of Engineers under Contract No. DACW 45-94-D-0001, Delivery Order 26, Project Number FXBM 98-7006, Rust Environmental & Infrastructure, January 1999.

21. "Airborne *MTADS* Demonstration on the Impact Area of the Badlands Bombing Range, September 2001," J. R. McDonald, David Wright, Nagi Khadr, and H. H. Nelson, NRL/PU/6110--02-453

Appendix A. Points of Contact

ESTCP		
Jeffrey Marqusee	ESTCP Director	Tel: 703-696-2120 Fax: 703-696-2114 Jeffrey.Marqusee@osd.mil
Anne Andrews	Program Manager, UXO	Tel: 703-696-3826 Fax: 703-696-2114 Anne.Andrews@osd.mil
Matthew Chambers	Program Assistant, UXO	Tel: 703-736-4508 Fax: 703-478-0526 chambers@hgl.com
NRL		
H. H. Nelson	Co-Investigator	Tel: 202-767-3686 Fax: 202-404-8119 herb.nelson@nrl.navy.mil
AETC, Inc.		
J.R. McDonald	Co-Investigator	Tel: 703-413-0500 Fax: 703-413-0512 jmcdonald@va.aetc.com
Tom Bell	Analyst	Tel: 703-413-0500 Fax: 703-413-0505 tbell@va.aetc.com
Bruce Barrow	Analyst	Tel: 703-413-0500 Fax: 703-413-0505 bjb@va.aetc.com
OST		
Emma Featherman-Sam	Director, Badlands Bombing Range Project	Tel: 605-867-1271 Fax: 605-867-5044
Ila Twiss	Director, OST Land Office	Tel: 605-867-5305 Fax: 605-867-5044
Kim Clausen	Director, Environmental Program	Tel: 605-867-5326 Fax: 605-867-5044
	Tribal Employment Office (TERO)	Tel: 605-867-5767

Ellsworth AFB

Dell Petersen	Environmental Office CIV 28 CES/CEVR	Tel: 605-385-2675 Fax: 605-385-6619 dell.petersen@ellsworth.af.mil
Larry Amburn	Environmental Office 28 CES/CEVR	Tel: 605-385-6616 Tel: 605-385-2680
Gary Schmidt	28 CES/CEVR	Tel: 605-385-2500 Fax: 605-385-6619 garyschmidt@ellsworth.af.mil

COE; Omaha

Len Havel	CENWO-PM-H	Tel: 402-221-7718 Fax: 402-221-7838

EPA: Region 8

Jeff Mashburn	Remedial Project Manager	Tel: 303-312-6665 Fax: 303-312-7047 mashburn.jeff@epa.gov

South Dakota Department of Environment and Natural Resources

Tony Anderson		Tel: 605-773-6477
Ron Holm		Tel: 605-773-6478

Nova Research, Inc.

Russell Jeffries	Logistics Support	Tel: 703-360-3900 Fax: 703-360-3911 Page: 703-518-1950 rjeffr@erols.com
Glenn Harbaugh	Site Safety Officer	Tel: 301-392-1702 Fax: 301-870-3130 Cell: 410-610-3506 harbaugh@ccs.nrl.navy.mil

EOTI, Inc

Wayne Lewallan	Senior UXO Supervisor	Tel: 732-345-8099 Fax: 732-345-7399 Cell: 732-492-1124 eoti@exit109.com

Appendix B. Data Archiving and Demonstration Plan

All survey data, a spreadsheet of model fit results, and a copy of the approved Demonstration Plan for this Demonstration are included on the CD attached to this report.

Appendix C. Model Fit Results

Table C1. Model Results for 105-mm projectiles

	Magnetometer Fit									3-β Fit											Constrained 3-β Fit										
ID	Local X (m)	Local Y (m)	Depth (m)	Size (m)	Inclin.	Az.	Fit Qual.	Comments	Cat.	Local X (m)	Local Y (m)	Depth (m)	Θ	Φ	Ψ	β_1	β_2	β_3	Fit Qual.	χ^2	Local X (m)	Local Y (m)	Depth (m)	Θ	Φ	Ψ	β_1	β_2	β_3	Fit Qual.	χ^2	S_1 (max)
13	389.49	548.04	0.66	0.125	71	261	0.952	poor degaussing?, 105, nose down	2	389.44	547.73	0.35	-37	61	-47	12.1	4.2	5.9	0.981	8373	389.52	547.88	0.53	88	42	46	16.8	11.8	11.8	0.966	15046	2859
59	538.57	579.57	0.74	0.147	82	170	0.975	good fit for a 155	1	538.61	579.46	0.45	46	-139	-15	10.0	7.0	3.8	0.972	3567	538.74	579.55	0.46	73	-60	-175	8.8	5.1	5.1	0.968	4368	1680
99	507.18	585.20	0.91	0.141	74	222	0.969	105, nose down	1	507.06	584.88	0.60	28	-106	122	9.2	3.1	0.0	0.938	2189	507.05	585.24	0.77	81	-127	-150	8.8	5.1	5.1	0.919	3636	626
133	474.58	656.87	0.67	0.117	55	251	0.960	105, slight remnant	2	474.67	656.84	0.37	24	47	-26	8.4	3.5	6.6	0.989	4528	474.52	656.78	0.42	62	-129	-168	8.8	5.1	5.1	0.969	13215	3222
142	512.94	679.83	0.61	0.101	34	30	0.954	105mm	1	512.92	679.85	0.31	-13	50	-125	8.4	5.2	6.5	0.980	6308	512.98	679.88	0.53	79	154	-54	16.8	11.8	11.8	0.965	11233	2432
149	460.22	689.48	0.69	0.138	51	312	0.982	105/155mm, E/W, nose down	1	460.41	689.39	0.37	65	-51	-112	6.4	4.4	5.6	0.977	2063	460.39	689.41	0.63	87	-1	-162	16.8	11.8	11.8	0.959	4566	1697
163	434.35	711.40	0.67	0.135	47	299	0.972	155mm, E/W	1	434.40	711.43	0.62	9	138	160	6.5	4.2	5.5	0.979	6577	434.39	711.39	0.89	85	95	133	16.8	11.8	11.8	0.968	11265	1913

Table C2. Model Results for 155-mm projectiles

	Magnetometer Fit									3-β Fit											Constrained 3-β Fit										
ID	Local X (m)	Local Y (m)	Depth (m)	Size (m)	Inclin.	Az.	Fit Qual.	Comments	Cat.	Local X (m)	Local Y (m)	Depth (m)	Θ	Φ	Ψ	β_1	β_2	β_3	Fit Qual.	χ^2	Local X (m)	Local Y (m)	Depth (m)	Θ	Φ	Ψ	β_1	β_2	β_3	Fit Qual.	χ^2	S_1 (max)
86	383.80	601.67	0.73	0.217	-69	282	0.950	totally inverted, fence post?	5	383.82	601.68	0.33	26	-111	-71	18.7	12.3	16.0	0.985	21187	383.79	601.77	0.57	71	157	53	40.6	28.8	28.8	0.973	38105	4482
88	429.63	581.65	0.86	0.204	75	355	0.947	good fit for 8in	1	429.67	581.65	0.43	15	-27	21	14.0	11.2	8.8	0.984	4818	429.69	581.67	0.49	20	-27	-78	16.8	11.8	11.8	0.982	5248	1984
104	539.83	624.56	0.85	0.164	31	28	0.974	155mm	1	539.95	624.51	0.43	5	-149	139	14.1	11.6	10.4	0.989	4608	540.02	624.56	0.47	29	22	-4	16.8	11.8	11.8	0.986	5893	2405
109	482.37	621.69	1.12	0.209	72	270	0.956	8-in, E/W	1	481.80	621.61	0.89	-23	-16	24	55.0	37.0	15.2	0.903	3469	481.95	621.85	0.70	16	123	-95	16.8	11.8	11.8	0.871	6584	901
121	367.38	636.27	0.92	0.092	44	4	0.867	clutter	6	367.60	635.55	0.46	11	-64	-119	6.0	2.4	1.3	0.889	2699	367.52	635.82	0.75	77	145	172	8.8	5.1	5.1	0.755	5386	599
132	441.28	657.90	0.57	0.132	45	316	0.983	likely 105	1	441.20	657.91	0.51	-31	-25	-120	17.4	12.7	15.4	0.993	9137	441.19	657.90	0.48	-45	-40	50	16.8	11.8	11.8	0.987	15631	5917
135	500.78	651.99	1.03	0.133	69	54	0.874	105-mm, nose down	1	500.70	651.86	0.64	37	-118	-166	19.8	10.9	14.6	0.986	2561	500.78	652.02	0.59	39	55	43	16.8	11.8	11.8	0.983	3052	1666
148	468.05	683.84	0.81	0.156	63	188	0.986	155mm	1	467.91	683.72	0.53	-9	-23	-167	25.8	8.4	15.3	0.984	10862	467.87	683.65	0.29	5	175	54	8.8	5.1	5.1	0.954	33511	3279
154	394.32	691.49	1.39	0.235	87	3	0.941	deep 8-in, nose down	1	394.14	691.43	1.05	-11	42	-77	23.6	9.5	4.3	0.913	2354	394.27	691.45	0.86	-8	35	149	8.8	5.1	5.1	0.862	3746	631
167	502.18	717.05	1.04	0.108	64	359	0.921	possible deep 105mm	2	502.10	716.87	1.00	1	17	-20	53.8	6.9	32.5	0.930	2239	502.26	717.06	1.00	14	39	32	40.6	28.8	28.8	0.877	4311	854

Table C3. Model Results for 8-in projectiles

	Magnetometer Fit									3-β Fit											Constrained 3-β Fit										
ID	Local X (m)	Local Y (m)	Depth (m)	Size (m)	Inclin.	Az.	Fit Qual.	Comments	Cat.	Local X (m)	Local Y (m)	Depth (m)	Θ	Φ	Ψ	β_1	β_2	β_3	Fit Qual.	χ^2	Local X (m)	Local Y (m)	Depth (m)	Θ	Φ	Ψ	β_1	β_2	β_3	Fit Qual.	χ^2	S_1 (max)
26	470.81	534.05	1.12	0.166	88	147	0.942	likely 155, nose down	1	470.92	534.06	0.66	25	12	-58	33.6	25.9	20.4	0.975	7905	470.96	534.03	0.73	41	18	-116	40.6	28.8	28.8	0.974	8554	2513
89	415.36	597.87	0.76	0.192	29	15	0.962	155mm/8in, good target	1	415.33	597.83	0.41	39	-152	-108	43.0	33.1	35.9	0.993	17584	415.30	597.82	0.38	30	-145	73	40.6	28.8	28.8	0.992	19930	9027
112	455.59	632.93	1.37	0.225	84	254	0.969	8-in deep	1	455.50	633.02	0.85	7	153	22	34.9	21.7	12.1	0.942	1726	455.67	632.84	1.01	10	-44	-113	40.6	28.8	28.8	0.886	3391	646
139	538.84	657.89	1.12	0.210	70	84	0.981	8-in, E/W	1	538.99	657.88	0.74	32	72	57	37.1	28.0	28.6	0.981	3808	539.00	657.90	0.75	35	71	54	40.6	28.8	28.8	0.981	3799	1965
153	405.62	686.54	1.24	0.148	90	356	0.970	probable deep 155	1	405.50	686.62	0.88	10	90	8	10.2	6.5	3.5	0.919	2374	405.47	686.57	1.13	7	93	-138	16.8	11.8	11.8	0.893	3024	603

Table C4. Model Results for frag clusters

	Magnetometer Fit									3-β Fit											Constrained 3-β Fit										
ID	Local X (m)	Local Y (m)	Depth (m)	Size (m)	Inclin.	Az.	Fit Qual.	Comments	Cat.	Local X (m)	Local Y (m)	Depth (m)	Θ	Φ	Ψ	β_1	β_2	β_3	Fit Qual.	χ^2	Local X (m)	Local Y (m)	Depth (m)	Θ	Φ	Ψ	β_1	β_2	β_3	Fit Qual.	χ^2	S_1 (max)
12	387.73	542.56	1.15	0.12	59	67	0.766	clutter pile	6	387.32	542.83	0.77	6	88	176	34.8	24.4	10.6	0.917	4292	387.40	542.78	0.70	2	80	-96	16.8	11.8	11.8	0.838	9194	832
21	448.97	546.51	1.06	0.109	63	121	0.745	low probability 105	3	448.62	547.19	0.41	-6	-87	-65	9.9	2.8	4.1	0.861	6280	448.68	547.22	0.48	12	93	9	8.8	5.1	5.1	0.792	9094	758
24	454.15	532.88	0.84	0.087	81	46	0.645	low probability 105	3	454.15	533.20	0.31	5	145	-180	5.5	3.5	0.8	0.915	2266	454.17	533.23	0.56	-13	-35	-38	8.8	5.1	5.1	0.767	5733	504
25	460.18	531.62	0.87	0.102	39	48	0.852	possibible 105	2	460.06	531.89	0.28	-3	30	179	2.9	1.8	0.8	0.874	3804	460.25	531.98	0.66	15	8	137	8.8	5.1	5.1	0.791	6084	489
27	467.59	538.91	0.77	0.114	34	193	0.799	possible 105	3	466.79	539.08	0.66	-10	165	-91	65.0	2.2	30.2	0.815	12298	467.59	539.03	0.51	11	92	-104	8.8	5.1	5.1	0.696	20294	995
28	477.95	547.73	1.10	0.148	25	39	0.642	likely clutter pile	5	477.76	547.74	0.87	7	-12	85	87.8	21.0	44.3	0.897	8581	477.49	547.82	0.82	30	-24	-75	40.6	28.8	28.8	0.729	46798	1279
31	482.95	551.70	0.94	0.094	75	90	0.825	likely clutter	6	483.23	551.89	0.60	-5	52	127	14.8	6.2	0.0	0.893	3448	483.19	551.90	0.54	30	-134	38	8.8	5.1	5.1	0.803	5701	539
32	484.79	546.70	1.12	0.111	54	64	0.859	clutter	6	484.52	547.61	0.57	-5	78	169	14.6	7.9	1.8	0.902	3099	484.74	547.99	0.86	11	110	68	16.8	11.8	11.8	0.681	9715	707
33	489.32	544.21	1.26	0.116	79	31	0.769	clutter	6	489.27	544.54	0.62	1	-107	99	16.9	5.3	11.8	0.883	2997	489.36	544.57	0.53	-1	62	-120	8.8	5.1	5.1	0.784	6952	609
35	507.54	530.73	1.10	0.121	48	43	0.706	clutter	6	507.21	530.71	0.65	-3	-114	-64	30.8	9.4	15.3	0.809	22536	507.29	530.62	0.86	11	87	-172	40.6	28.8	28.8	0.752	29891	1262
55	558.03	550.36	0.59	0.08	59	320	0.895	small end of a 105	3	557.51	550.38	0.58	4	-178	-163	26.5	17.8	4.0	0.868	13330	557.92	550.29	0.98	19	40	150	40.6	28.8	28.8	0.744	24309	1012
56	560.78	554.52	0.76	0.097	55	346	0.902	possible 105, 22 ft E of site	3	560.54	554.86	0.69	21	72	85	21.5	5.9	15.8	0.773	10249	560.56	554.75	0.99	33	59	-86	40.6	28.8	28.8	0.738	12279	992
66	479.21	563.93	0.80	0.091	65	35	0.881	posible 105	3	479.20	564.03	0.29	0	50	-79	4.3	1.3	2.2	0.942	2789	479.19	564.10	0.55	3	56	49	8.8	5.1	5.1	0.898	4835	750
78	433.75	567.27	0.66	0.071	48	62	0.881	unlikely UXO	5	433.39	567.57	0.54	3	99	7	9.1	7.2	2.3	0.754	3875	433.43	567.29	0.92	24	-25	157	16.8	11.8	11.8	0.585	6350	421
134	495.47	643.93	0.65	0.097	46	58	0.892	low probability 105	3	495.37	643.96	0.43	22	14	-3	10.3	8.9	1.9	0.885	9076	495.12	643.89	0.45	3	103	-73	8.8	5.1	5.1	0.806	16835	1165
150	447.43	675.04	1.20	0.147	89	105	0.887	possible deep 155	2	447.38	675.30	0.83	-5	-21	87	17.9	5.0	11.0	0.942	3722	447.42	675.35	1.27	22	125	103	40.6	28.8	28.8	0.881	7550	926
157	364.18	729.66	0.84	0.123	79	65	0.897	possible 105 on N border	3	364.21	730.09	0.68	4	114	-176	11.5	7.7	1.3	0.900	6656	364.17	729.99	0.91	6	130	-39	16.8	11.8	11.8	0.809	12025	937
159	377.14	704.99	0.88	0.11	47	38	0.881	low probability 105	3	376.96	704.91	0.79	-2	101	176	7.9	6.1	1.7	0.893	3906	377.02	704.88	0.95	-12	93	91	8.8	5.1	5.1	0.778	6759	548
162	409.94	719.57	1.16	0.121	36	45	0.880	likely not UXO	4	409.94	719.60	0.98	4	-14	178	19.9	15.1	3.9	0.872	3258	409.91	719.61	1.09	15	-36	-77	16.8	11.8	11.8	0.719	9710	514

Table C5. Model Results for single frag items

	Magnetometer Fit									3-β Fit											Constrained 3-β Fit										
ID	Local X (m)	Local Y (m)	Depth (m)	Size (m)	Inclin.	Az.	Fit Qual.	Comments	Cat.	Local X (m)	Local Y (m)	Depth (m)	Θ	Φ	Ψ	β_1	β_2	β_3	Fit Qual.	χ^2	Local X (m)	Local Y (m)	Depth (m)	Θ	Φ	Ψ	β_1	β_2	β_3	Fit Qual.	χ^2	S_1 (max)
29	479.96	541.89	0.38	0.065	34	54	0.980	too small for 105	6	480.08	541.83	-0.05	35	24	-99	0.5	0.1	0.0	0.925	5375	480.19	541.63	0.75	77	57	-161	8.8	5.1	5.1	0.651	23975	712
38	519.79	531.82	0.79	0.098	41	5	0.721	possible 105 in clutter	3	520.00	531.59	0.26	34	87	-42	2.1	1.3	1.6	0.879	7960	519.98	531.55	0.66	85	-9	140	8.8	5.1	5.1	0.868	9583	743
54	556.80	549.73	0.37	0.077	68	14	0.911	small end of 105	3	556.83	549.95	0.41	-21	-96	-6	13.4	9.8	3.9	0.928	14276	556.79	549.84	0.55	22	95	148	16.8	11.8	11.8	0.878	24210	1913
93	415.39	592.89	1.14	0.113	87	219	0.883	unlikely 105	3	415.11	593.38	0.37	0	-29	-98	9.4	1.9	5.9	0.879	8059	415.11	593.24	0.69	-3	130	68	16.8	11.8	11.8	0.799	12420	753
95	440.20	583.48	0.42	0.060	39	4	0.753	too small	6	440.05	583.58	0.00	23	97	-68	0.9	0.4	0.0	0.955	2865	440.12	583.49	0.73	70	65	-175	8.8	5.1	5.1	0.674	22434	687
98	481.95	600.68	0.49	0.060	48	356	0.856	too small	6	481.99	600.52	0.02	-13	25	178	1.1	0.1	0.3	0.884	2843	482.26	600.34	0.60	46	-146	1	8.8	5.1	5.1	0.658	9234	559
101	551.01	585.66	0.73	0.090	22	12	0.904	possible 105	2	551.05	586.08	0.46	-6	69	142	11.8	2.7	0.9	0.905	4129	551.15	586.29	0.58	-21	69	-111	8.8	5.1	5.1	0.707	11760	774
107	480.20	634.17	1.00	0.121	35	14	0.892	possible 105	2	479.82	634.16	0.69	0	-122	-17	28.1	17.4	5.5	0.814	6592	479.86	634.26	0.69	8	99	-85	16.8	11.8	11.8	0.627	18173	798
128	402.60	649.59	0.94	0.104	74	224	0.905	multiple targets	5	402.74	649.98	0.70	-5	-48	66	22.6	4.7	14.9	0.901	3226	402.72	649.68	0.77	-2	-20	-125	16.8	11.8	11.8	0.839	6128	704
130	430.05	664.55	0.35	0.047	89	70	0.831	too small	6	429.97	664.41	0.20	-49	79	54	1.5	0.1	0.6	0.981	860	430.17	664.65	0.70	79	-138	59	8.8	5.1	5.1	0.828	10019	815
140	561.99	655.22	0.37	0.066	80	226	0.952	too small, outside site	6	562.37	654.95	0.22	-30	124	48	3.5	0.0	0.0	0.916	5830	562.09	655.27	0.68	64	-77	61	8.8	5.1	5.1	0.642	26640	882
143	507.27	686.48	0.36	0.049	45	1	0.797	trash	6	507.24	686.51	0.12	-41	-51	-153	1.3	0.1	0.2	0.958	2204	507.40	686.28	0.78	90	-158	-171	8.8	5.1	5.1	0.688	21227	860

Table C6. Model Results for scrap items

	Magnetometer Fit									3-β Fit											Constrained 3-β Fit										
ID	Local X (m)	Local Y (m)	Depth (m)	Size (m)	Inclin.	Az.	Fit Qual.	Comments	Cat.	Local X (m)	Local Y (m)	Depth (m)	Θ	Φ	Ψ	β_1	β_2	β_3	Fit Qual.	χ^2	Local X (m)	Local Y (m)	Depth (m)	Θ	Φ	Ψ	β_1	β_2	β_3	Fit Qual.	χ^2	S_1 (max)
47	541.64	534.72	0.96	0.158	73	306	0.845	155 or 8in deep, large clutter on top	2	541.96	535.37	0.59	-8	33	82	52.8	15.7	36.2	0.894	49779	542.11	535.43	0.62	13	29	-147	40.6	28.8	28.8	0.826	98513	3231
48	544.28	535.12	0.35	0.074	5	25	0.941	likely clutter	5	544.82	534.90	0.33	-7	95	-176	14.3	8.8	2.9	0.678	133241	544.81	534.91	0.72	-5	112	-173	40.6	28.8	28.8	0.587	168772	2044
90	431.30	595.78	0.37	0.095	14	43	0.919	shallow 105	1	431.34	595.81	0.08	12	49	97	4.2	0.7	1.4	0.973	5382	431.29	595.73	0.36	2	38	-40	8.8	5.1	5.1	0.758	52957	1770
94	435.97	588.71	0.38	0.055	11	52	0.940	trash	6	436.09	588.58	0.03	7	24	25	1.1	0.2	0.0	0.915	2819	436.05	588.54	0.65	8	19	134	8.8	5.1	5.1	0.412	19932	674
116	413.49	616.89	0.38	0.085	17	350	0.957	low end of 105mm	1	413.58	616.90	0.10	4	101	23	4.4	0.1	1.2	0.967	7980	413.74	616.87	0.49	86	106	160	8.8	5.1	5.1	0.673	78485	1869
168	523.52	700.80	0.33	0.084	24	30	0.936	possible shallow 105mm	2	523.50	700.83	0.06	-52	11	-96	3.7	1.1	2.5	0.984	9203	523.61	700.90	0.26	-63	-122	-151	8.8	5.1	5.1	0.955	26602	4058